ISSN: 2153-1196 Volume 13, Number 3, March 2022

Scientific Research Publishing

Journal of Modern Physics

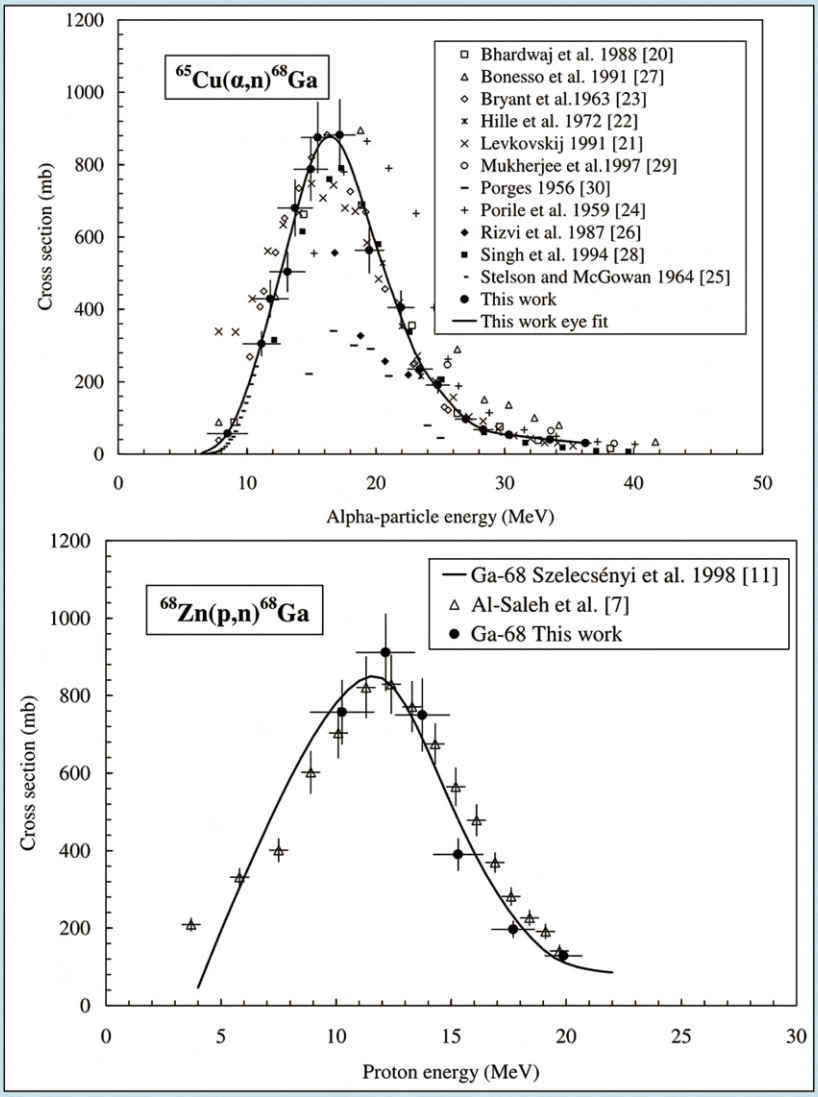

ISSN: 2153-1196

https://www.scirp.org/journal/jmp

Journal Editorial Board

ISSN: 2153-1196 (Print) ISSN: 2153-120X (Online)
https://www.scirp.org/journal/jmp

Editor-in-Chief

Editorial Board

Scientific Research Publishing

Journal of Modern Physics, 2022, 13, 267-322
https://www.scirp.org/journal/jmp
ISSN Online: 2153-120X
ISSN Print: 2153-1196

Table of Contents

Volume 13 Number 3 March 2022

The figure on the front cover is from the article published in Journal of Modern Physics, 2022, Vol. 13, No. 3, pp. 267-273 by Papa Mady Sy and Mounibé Diarra.

Journal of Modern Physics (JMP)
Journal Information

SUBSCRIPTIONS

The *Journal of Modern Physics* (Online at Scientific Research Publishing, https://www.scirp.org/) is published monthly by Scientific Research Publishing, Inc., USA.

Subscription rates:
Print: $89 per issue.
To subscribe, please contact Journals Subscriptions Department, E-mail: sub@scirp.org

SERVICES

Advertisements
Advertisement Sales Department, E-mail: service@scirp.org

Reprints (minimum quantity 100 copies)
Reprints Co-ordinator, Scientific Research Publishing, Inc., USA.
E-mail: sub@scirp.org

COPYRIGHT

PRODUCTION INFORMATION

For manuscripts that have been accepted for publication, please contact:
E-mail: jmp@scirp.org

Journal of Modern Physics, 2022, 13, 267-273
https://www.scirp.org/journal/jmp
ISSN Online: 2153-120X
ISSN Print: 2153-1196

Production of Gallium-68 with Medium to Low Energy Cyclotrons: What Opportunities for the Development of PET Radiotracers in Senegal?

Papa Mady Sy*, Mounibé Diarra*

Laboratory of Physics and Pharmaceutical Biophysics, Faculty of Medicine, Pharmacy and Odontology, UCAD, Dakar, Senegal
Email: *papamady.sy@ucad.edu.sn, *mounibe.diarra@ucad.edu.sn

How to cite this paper: Sy, P.M. and Diarra, M. (2022) Production of Gallium-68 with Medium to Low Energy Cyclotrons: What Opportunities for the Development of PET Radiotracers in Senegal? *Journal of Modern Physics*, **13**, 267-273.
https://doi.org/10.4236/jmp.2022.133018

Received: January 28, 2022
Accepted: February 27, 2022
Published: March 2, 2022

Abstract

This study focuses on the development possibilities of radiotracers used in PET in Senegal. This is a literature review that develops the production of 68-Gallium (^{68}Ga[Ga]) via a medium to low energy cyclotron. It shows the possibility of producing ^{68}Ga[Ga] with a simple production reaction using a target of ^{68}Zn. This reaction provides high production yields, at the end of the bombardment (EOB), reaching up to 80 times the activity of a generator. PET imaging may offer better sensitivity and spatial resolution compared to SPECT which is currently used in Senegal. The acquisition of this type of medium to low energy accelerator in Senegal may constitute an important phase in the development of radiotracers with the objective of installing a PET imaging. However, solutions must be provided to minimize the presence of isotopic impurities.

Keywords

Gallium-68, PET, Radiotracers, Cyclotron, Senegal

1. Introduction

Gallium (Ga) is a chemical element belonging to the family of post-transition metals (group 13 of the periodic table of the elements). It is a silvery-looking metal with a melting point of 29.8˚C [1] [2]. Gallium has two stable isotopes, ^{69}Ga and ^{71}Ga (61.1% and 39.9% of natural gallium, respectively). ^{68}Ga [Ga] (physical half-life of 67.71 minutes) combines two decay modes: electron capture (10% to 12%) and beta + decay (88 to 90%) (Table 1) to give ^{68}Zinc.

The β+ type decay results in the emission of a positron allowing the formation of two annihilation photons, essential for PET (positron emission tomography) imaging [1] [3] [4].

Table 1. Main emissions of ^{68}Ga[Ga] [1] [3] [4].

Gallium 68	
Gamma emission	$\gamma_{\text{annihilation}} = 511\ \text{keV};\ \gamma_{\text{transition}} = 1077.34\ \text{keV}(3.22\%)$
β+	$E_{\beta\text{moy}} = 836\ \text{keV};\ E_{\beta\max} = 1899\text{keV}$

While PET is becoming more and more accessible, ^{68}Ga [Ga] has the advantage of being a metal and therefore of offering possibilities different from those of halogens, by its way of binding to other atoms (chemistry of coordination), which makes it more versatile.

Currently, ^{68}Ga [Ga] is mainly produced from a ^{68}Ge[Ge]/^{68}Ga[Ga] generator. The ^{68}Ge[Ge]/^{68}Ga[Ga] generator remains practical, because it guarantees the supply of ^{68}Ga [Ga] for several months (^{68}Ge[Ge] physical period: 270.82 days). However, the use of the generator can be limited by its activity (typically 1.85 GBq of nominal activity when new); the minimum interval between elutions (typically 3 - 4 hours); the elution efficiency (~60% - 80%); and the potential for the parent radionuclide to be long-lived (^{68}Ge[Ge]) crosses the column and ends up in the eluate (breakthrough) [5] [6] [7] [8].

Taking these considerations into account, Jensen and Clark [9] have developed an innovative method to meet the growing demand for ^{68}Ga[Ga]. This method consisted in producing ^{68}Ga[Ga] via a cyclotron with a liquid target consisting of a solution of $^{68}ZnCl_2$ [9]. Since then, other research groups have attempted to optimize the production of ^{68}Ga[Ga] with a liquid target [5] [10]. Although the production of ^{68}Ga[Ga] via a liquid target is facilitated by the target preparation process, the activity of ^{68}Ga[Ga] available at the end of production is not significantly higher than that produced by the generator. To overcome the limitations seen with the use of a liquid target, a solid (enriched) target can dramatically improve the overall production of ^{68}Ga[Ga]. Precisely, the objective of this bibliographical synthesis is therefore to highlight the production of ^{68}Ga[Ga] via a cyclotron by the use of a solid target (nature of the target, irradiation and production rate, quality of the radioelement produced, various impurities observed…).

2. Ways of Producing ^{68}Ga[Ga] from a cyclotron, Medium to Low Energy

Several methods of producing ^{68}Ga[Ga] have been developed using cyclotrons. Considering the type of particles typically accelerated in medium to low energy accelerators, four reactions can efficiently produce ^{68}Ga[Ga], namely:

^{65}Cu (α, n) ^{68}Ga on a copper target, **^{68}Zn (p, n) ^{68}Ga, ^{68}Zn (d, 2n) ^{68}Ga and ^{70}Zn (p, 3n) ^{68}Ga** on zinc targets [11] [12].

According to evaluations by Szelecsényi and al. and Sadeghi *et al.* [11] [13] based on the study of the cross section (maximum values of the cross sections: 882.0 ± 98.5 milli-barns for 17.2 ± 1.2 MeV with α particle on ^{65}Cu[Cu] target et 911.3 ± 99.4 milli-barns for 12.2 ± 1.3 MeV with a proton on ^{68}Zn target)

(Figure 1), the reactions **^{65}Cu (α, n) ^{68}Ga** and **^{68}Zn (p, n) ^{68}Ga** are the best to produce ^{68}Ga[Ga] from of a medium to low energy accelerator.

In addition, among these two nuclear reactions, the irradiation of Zn by protons (**^{68}Zn[Zn] (p, n) ^{68}Ga[Ga]**) is the preferred one (the one we have also chosen) according to several studies because it leads to a higher production yield with less impurities and uses protons, the simplest of all cyclotron projectiles [5] [11] [13] [15].

3. Production of ^{68}Ga[Ga] via a Cyclotron Using a Solid Target of ^{68}Zn[Zn]

3.1. Nature of the Target

Aiman H. Alnahwi *et al.* [16] developed an automated ^{68}Ga[Ga] radiosynthesis for routine large-scale production using a squeezed ^{68}Zn[Zn] target (target highly enriched to 99.26 in ^{68}Zn[Zn]) (Table 2).

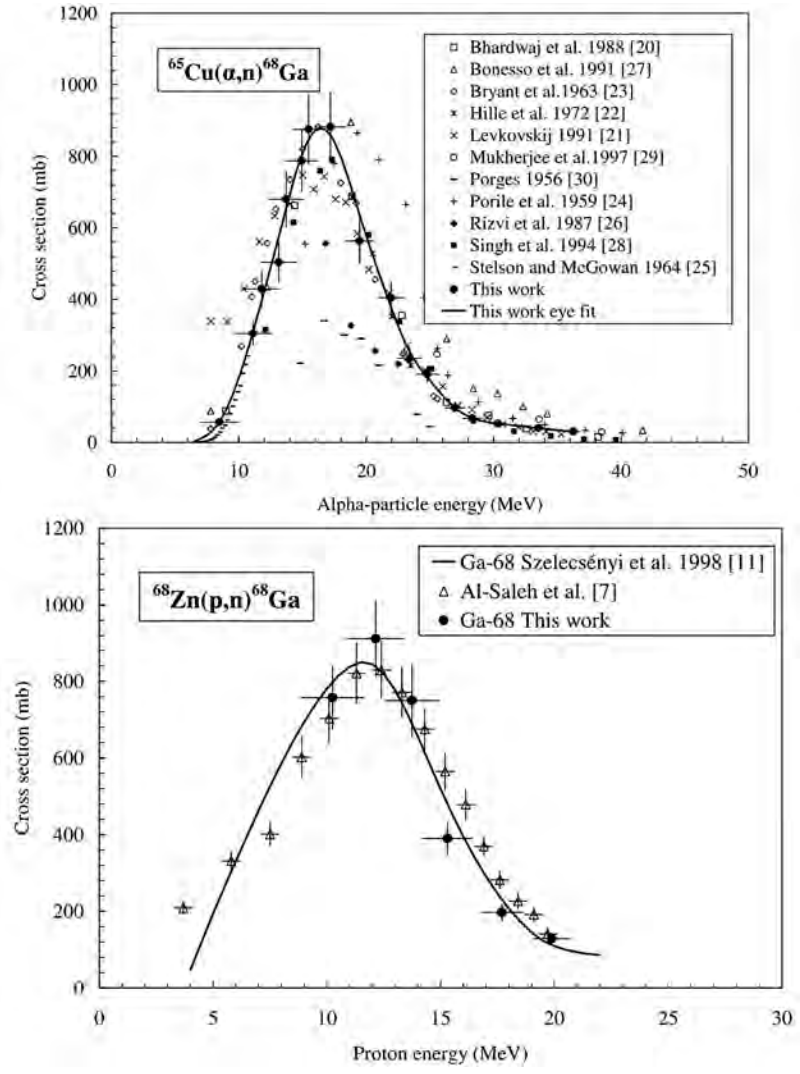

Figure 1. Cross sections of reactions ^{65}Cu[Cu] (α, n) ^{68}Ga[Ga] and ^{68}Zn[Zn] (p, n) ^{68}Ga[Ga] [11] [14].

Table 2. Isotopic composition of the target and impurities [16].

Zn (%)	^{64}Zn (0.01)	^{66}Zn (0.1)	^{67}Zn (0.61)	^{68}Zn (99.26)	^{70}Zn (0.02)			
Impureties (ppm)	Al (<1)	Cu (5.3)	Fe (220)	Cr (20.3)	Sn (170)	Co (<1)	Ca (<5)	Cd (125)
	Pb (3.6)	As (<0.1)	Si (4)	Mg (1.8)	Mn (1.17)	K (13)	Na (2.7)	

Thus, ^{68}Zn[Zn] pellets of different diameter and thickness were prepared (diameter: 6 to 10 mm and thickness: 0.51 to 0.55 mm). The target carrier was made of aluminum, so it was only weakly activated by the proton beam from the cyclotron according to these authors. In addition, aluminum, due to its thermal conductivity properties [17] [18], allowed efficient cooling of the target during irradiation.

In another study, Lin *et al.* [8] used an enriched ^{68}Zn[Zn] target (60 - 120 mg) with a diameter of 7 mm. The target was electrodeposited on a platinum disc and then it was transferred and mounted in the cyclotron PETtrace via the module Comecer EDS/PTS (Castel Bolognese RA, Italy).

3.2. Target Irradiation and Production Efficiency

Aiman H. Alnahwi *et al.* [16] used irradiations with a beam current between 5 and 35 μA on the squeezed ^{68}Zn[Zn] target with an energy ranging from 13 to 14.5 MeV for a duration of 90 minutes. The irradiations were first carried out on a 6 mm target for which the production yield (corrected for the decay) was 2.6 GBq/μA·h. The activity of ^{68}Ga[Ga] increased when the current applied to the target was greater (input 1 - 3). The highest production yields were obtained with the 8- and 10-mm targets (entries 4 - 5). Using a current of 35 μA, 145 ± 6 GBq (at EOB: end of bombardment) was produced (input 6) (**Table 3**). This value (145 ± 6 GBq in EOB) is superior to the values reported by Lin *et al.* (Lin, Waligorski, et Lepera 2018) which used an incident energy of 14.5 MeV proton beam with beam currents of 15 à 40 μA and a power equivalent to about 80 times the activity of a generator.

Other authors like Sadeghi *et al.* [13] obtained interesting yield values for the ^{68}Zn[Zn] (p, n) ^{68}Ga[Ga] nuclear reaction using a solid target of Zn enriched to 97% in ^{68}Zn[Zn]. Their EOB yield reached 5.032 GBq/μAh at 15 MeV with the use of a target of 52 μm thick; with an irradiation time of 0.25 h and a beam current of 150 μA. Szelecsényi *et al.* [11] reported that their values, calculated with the cross sections (5.809 GBq/μAh), were in agreement with these data.

3.3. Dissolving the Target

After facilitated transport via magnetic media (Automated Target Transfer System [12]), immediate dissolution of the target should be performed for rapid transfer to the purification column. 7N nitric acid HNO_3 can be used for target dissolution. Another particularly interesting method for extracting radioisotopes of gallium from zinc targets is the thermal diffusion method described by Tolmachev and Lundqvist [19]. A similar method was also employed by Zeisler *et al.* [20].

Table 3. Production yields [8] [16].

Entry	Pressed target diameter (mm)	Energy Ep (MeV)	Maximum current on target (μA)	Activity (GBq)[b]	Production yield (GBq/μA·h)	Saturation yield (GBq/μA)
1	6	14	5	7.2	2.6	5.1
2	6	14	12	17.0	2.2	4.3
3	6	14	25	32.8	2.6	5.0
4	8	14	15	36.6	4.8	9.0
5	10	14	30	68.6	4.6	8.7
6	10	13	35[c]	144.8 ± 6.4	2.7 ± 0.1	6.8 ± 0.1
7 (Lin)	7	14.5	30	60.9 ± 1.8	2.7 ± 0.1	5.6 ± 0.2[d]

[a]The proton beam energies were calculated by Monte Carlo simulation using SRIM. Irradiation time was fixed at 30 min. [b]Total recovered activity, corrected at EOB. [c]Irradiation time was 90 min. [d]Saturation yield estimated from results reported by Lin *et al.* [8]. Entries 1 - 5, n = 1; entry 6, n = 2.

3.4. Purification of ^{68}Ga[Ga]

The automated purification process implemented by Aiman H. Alnahwi *et al.* [16] used a hydroxamate resin. 0.01 N HCl solution (50 mL) was required to remove ^{68}Zn[Zn]. The ^{68}Ga[Ga] was then eluted from the hydroxamate resin with 0.75 N HCl as [^{68}Ga] $GaCl_3$. This provides ^{68}Ga[Ga] with a high radiochemical yield and a lead time of the dissolution and purification method of less than 10 - 12 min (20 min for Lin *et al.* [8]). The last purification step, carried out with the CUBCX resin [21], has already been validated internally.

3.5. Metallic and Isotopic Impurities

Aiman H. Alnahwi *et al.* [16] described the presence of metal impurities after purification. For all batches tested, metallic impurities were below the general limit of 10 ppm and 20 ppm for heavy metals (USP and Ph. Eur.). The concentrations of impurities of antimony, barium, beryllium, bismuth, cadmium, chromium, cobalt, lead, lithium, molybdenum, selenium, silver, tin, titanium, vanadium were <0.5 ppm. The elements Al, Fe, Mg, Zn and Cu were <4 ppm.

The main isotopic impurities were identified by gamma spectrometry (29, 50 and 72 h post purification) and consisted of ^{67}Ga[Ga] (physical period: 3.26 days) and ^{66}Ga[Ga] (physical period: 9.45 h), as indicated previously by Al-Saleh *et al.* [22] [23] and their total combined amount was less than 2% at 6 h after irradiation (Energy 13 MeV). ^{67}Ga[Ga] can be produced via the reactions ^{67}Zn[Zn] (p, n) ^{67}Ga[Ga] and ^{68}Zn[Zn] (p, 2n) ^{67}Ga[Ga] with incident proton energy of 2 - 26 MeV and 13 - 29.5 MeV, respectively. ^{66}Ga[Ga] can be produced via ^{66}Zn[Zn] (p, n) ^{66}Ga[Ga] and ^{67}Zn[Zn] (p, 2n) ^{66}Ga[Ga] with incident particle energy of 6 - 26 MeV and 15 - 26 MeV, respectively [24]. According to the experimental measurements reported by Alves *et al.* [5], the amounts of ^{67}Ga[Ga] and ^{66}Ga[Ga] can be kept below 2% using a particle energy of 13 MeV. For example, the

^{68}Ga[Ga] purities may be 99.97% and 99.99% at EOB for particle energies of 14 and 13 MeV respectively. These values were confirmed by Lin *et al.* [8] who observed a small fraction (≤0.2%) of ^{67}Ga[Ga] when the target was irradiated for up to 90 min with 14.5 MeV protons.

3.6. Target Recovery

Many authors have not performed a target recovery process, believing it to be more expensive than buying a new target. However, according to an IAEA document [12], ^{68}Zn[Zn] can easily be recovered provided no impurities (e.g. iron) are present. Thus, simple multiple drying with nitric acid can be performed as described below. The procedure includes: 1) dry evaporation; 2) Dilution in concentrated nitric acid (>10 M); 3) Repeat the evaporation; 4) Dilution in 10 mM nitric acid; and 5) Evaporation to dryness or preparation of a ready-to-use solution. >90% recovery of the ^{68}Zn isotope of Zinc is expected. All reagents used must be of high quality, traces of metal.

Buying a new target is worth more than this long and tedious target recovery process.

4. Conclusion

The acquisition of a medium to low energy cyclotron can be a huge opportunity for developing African countries including Senegal. The production technique is quite accessible. Obtaining gallium could initiate the development of new PET radiotracers hitherto unused, particularly ^{68}Ga[Ga]-PSMA (prostate specific membrane antigen), now essential in the diagnosis of prostate cancer. The objective of developing these radiotracers and the installation of a PET are today major challenges and issues for Senegal. Thus, the production of ^{68}Ga[Ga] via a cyclotron therefore constitutes an innovative and interesting method with high production yields. However, it must be optimized to reduce or even eliminate isotopic impurities.

Conflicts of Interest

The authors declare no conflicts of interest regarding the publication of this paper.

References

[1] Casagrande, K. (2018) 68Ga-PSMA-11, nouveau traceur TEP pour l'imagerie du cancer de la prostate: Synthèse, contrôles qualité et dossier d'autorisation. Exercice, Université Toulouse III—Paul Sabatier.

[2] Downs, A.J. (1993) *Ch*emistry of Aluminium, Gallium, Indium and Thallium. Springer Science & Business Media, Berlin. https://doi.org/10.1007/978-94-011-2170-5

[3] Velikyan, I. (2015) *Molecules*, **20**, 12913-12943. https://doi.org/10.3390/molecules200712913

[4] Baldik, R. and Dombayci, A. (2016) *Applied Radiation and Isotopes*, **113**, 10-17.

https://doi.org/10.1016/j.apradiso.2016.04.002

[5] Alves, F., *et al.* (2017) *AIP Conference Proceedings*, **1845**, Article ID: 020001. https://doi.org/10.1063/1.4983532

[6] IAEA (2010) Production of Long Lived Parent Radionuclides for Generators: ^{68}Ge, ^{82}Sr, ^{90}Sr and ^{188}W. International Atomic Energy Agency, Vienna.

[7] Belosi, F., *et al.* (2013) *Current Radiopharmaceuticals*, **6**, 72-77. https://doi.org/10.2174/1874471011306020002

[8] Lin, M., Waligorski, G.J. and Lepera, C.G. (2018) *Applied Radiation and Isotopes*, **133**, 1-3. https://doi.org/10.1016/j.apradiso.2017.12.010

[9] Jensen, M. and Clark, J. (2011) Direct Production of Ga-68 from Proton Bombardment of Concentrated Aqueous Solutions of [Zn-68] Zinc Chloride. *The* 13*th International Workshop on Targetry and Target Chemistry Proceedings*, Roskilde, 26-28 July 2010, 288-292. https://orbit.dtu.dk/en/publications/direct-production-of-ga-68-from-proton-bombardment-of-concentrate

[10] Pandey, M.K., Byrne, J.F., Jiang, H., Packard, A.B. and DeGrado, T.R. (2014) *American Journal of Nuclear Medicine and Molecular Imaging*, **4**, 303-310.

[11] Szelecsényi, F., Kovács, Z., Nagatsu, K., Fukumura, K., Suzuki, K. and Mukai, K. (2012) *Radiochimica Acta*, **100**, 5-11. https://doi.org/10.1524/ract.2011.1896

[12] IAEA (2019) Gallium-68 Cyclotron Production. IAEA, Vienna.

[13] Sadeghi, M., Kakavand, T., Mokhtari, L. and Gholamzadeh, Z. (2009) *Pramana*, **72**, 335-341. https://doi.org/10.1007/s12043-009-0029-4

[14] Tárkányi, F.T., *et al.* (2019) *Journal of Radioanalytical and Nuclear Chemistry*, **319**, 533-666. https://doi.org/10.1007/s10967-018-6380-5

[15] Gilly, L.J., Henriet, G.A., Alves, M.P. and Capron, P.C. (1963) *Physical Review*, **131**, 1727-1731. https://doi.org/10.1103/PhysRev.131.1727

[16] Alnahwi, A.H., Tremblay, S., Ait-Mohand, S., Beaudoin, J.-F. and Guérin, B. (2020) *Applied Radiation and Isotopes*, **156**, Article ID: 109014. https://doi.org/10.1016/j.apradiso.2019.109014

[17] Alnahwi, A.H., Tremblay, S. and Guérin, B. (2018) *Applied Sciences*, **8**, 1579. https://doi.org/10.3390/app8091579

[18] Lin, M., Mukhopadhyay, U., Waligorski, G.J., Balatoni, J.A. and González-Lepera, C. (2016) *Applied Radiation and Isotopes*, **107**, 317-322. https://doi.org/10.1016/j.apradiso.2015.11.016

[19] Tolmachev, V. and Lundqvist, H. (1996) *Applied Radiation and Isotopes*, **47**, 297-299. https://doi.org/10.1016/0969-8043(95)00290-1

[20] Zeisler, S., Limoges, A., Kumlin, J., Siikanen, J. and Hoehr, C. (2019) *Instruments*, **3**, 10. https://doi.org/10.3390/instruments3010010

[21] Mueller, D., Klette, I., Baum, R.P., Gottschaldt, M., Schultz, M.K. and Breeman, W.A.P. (2012) *Bioconjugate Chemistry*, **23**, 1712-1717. https://doi.org/10.1021/bc300103t

[22] Al-Saleh, F.S., Al Mugren, K.S. and Azzam, A. (2007) *Applied Radiation and Isotopes*, **65**, 1101-1107. https://doi.org/10.1016/j.apradiso.2007.05.004

[23] Engle, J.W., *et al.* (2012) *Applied Radiation and Isotopes*, **70**, 1792-1796. https://doi.org/10.1016/j.apradiso.2012.03.030

[24] Szelecsényi, F., Boothe, T.E., Takács, S., Tárkányi, F. and Tavano, E. (1998) *Applied Radiation and Isotopes*, **49**, 1005-1032. https://doi.org/10.1016/S0969-8043(97)10103-8

Journal of Modern Physics, 2022, 13, 274-284
https://www.scirp.org/journal/jmp
ISSN Online: 2153-120X
ISSN Print: 2153-1196

Huge Variety of Nuclides That Arise in the LENR Processes: Attempt at Explanation

Alexander G. Parkhomov[1], Ekaterina O. Belousova[2]

[1]Russian Academy of Natural Sciences, Moscow, Russia
[2]Institute of Experimental Mineralogy, Russian Academy of Sciences, Moscow, Russia
Email: alexparh@mail.ru

How to cite this paper: Parkhomov, A.G. and Belousova, E.O. (2022) Huge Variety of Nuclides That Arise in the LENR Processes: Attempt at Explanation. *Journal of Modern Physics*, **13**, 274-284.
https://doi.org/10.4236/jmp.2022.133019

Received: January 29, 2022
Accepted: March 5, 2022
Published: March 8, 2022

Abstract

Researches in the field of low-energy nuclear reactions (LENR) have shown a wide variety of manifestations of these phenomena. They appear in metals with hydrogen dissolved in them, in plasma, in gas discharge, in electrolysis, and even in biological systems. In addition to energy release, which far exceeds the capabilities of chemical reactions, LENR is characterized by a huge variety of emerging chemical elements. This report provides examples of appearance of many initially missing elements in different LENR installations. For example, in the nickel-hydrogen LENR reactor created in our laboratory, which worked for 7 months, Ca, V, Ti, Mn, Fe, Co, Cu, Zn, Ga, Ba, Sr, Yb, Hf were found. Moreover, new elements were found not only in the "fuel" but also in the surrounding matter. The huge variety of chemical elements that arise can be explained by the fact that in the processes of LENR, the interaction covers several atoms at once. The article discusses approaches to explaining the phenomena discovered in the process of LENR researches.

Keywords

Nuclear Transmutations, LENR, Coulomb Barrier, Multicore Transformations, Hot Metals, Particles Collisions, Weak Nuclear Interaction, Neutrino, Low Energies

1. Introduction

This article gives special attention to an important feature of LENR: huge variety of emerging new nuclides. In the experiments of M. Fleischmann and S. Pons, which began intensive research in the field of LENR, tritium and helium were presumably formed during the fusion of deuterium nuclei. But soon it was discovered that cold nuclear transformations are not limited only to the fusion of

light nuclides. This paper provides a few examples of the various nuclear transformations found in various numerous experiments.

2. Examples of Huge Variety of Emerging New Nuclides

Experiments by I.B. Savvatimova, A.B. Karabut and Y.R. Kucherov [1] [2] began almost immediately after the publication by M. Fleischmann and S. Pons. In these experiments, the effect of a glow discharge in a medium of deuterium and other gases on palladium and other metals was investigated. Release of excess energy and many initially absent chemical elements were found. For instance, Sc, Ti, V, Ag, Cd, In, P, Cl, Br, Ge, As, Kr, Sr, Y, Ru, Xe were found in Pd. In some elements an unusual ratio of isotopes was found. In addition, gamma and neutron radiation was detected, as well as the appearance of radioactivity in the irradiated targets. However, detected radiation intensity and radioactivity were very weak. Thus, already in these early studies, many important properties of LENR were identified.

At the same time, in Magnitogorsk State Technical University, Anatoly Vachaev created an installation called "Energoniva" [3]. In this installation, water flowed between tubular electrodes, between which a special type of electric discharge was created. As a result, many elements that were initially absent appeared in the water, from lithium to lead. Most of all, iron appeared. In addition, heavy and superheavy water accumulated in the water, *i.e.* deuterium and tritium appeared. Vachaev's installation was reproduced in several laboratories. The appearance of many initially absent nuclides occurred everywhere.

Many initially absent nuclides from boron to lead were recorded in the well-known experiments of Leonid Urutskoev with exploding metal foils [4]. A change in the isotopic composition of titanium after an electric explosion was detected. In addition, in these experiments, "strange radiation" was detected, which formed unusual tracks in the photo emulsion and on the surfaces of various detectors [4] [5].

In the experiments of Ubaldo Mastromatteo [6] and Jean-Paul Biberian [7], palladium foils were subjected to prolonged laser irradiation in an atmosphere of hydrogen and deuterium. In the field of irradiation, many new chemical elements (N, O, Na, Mg, Al, S, Ca, Fe, Ni, Zn, Mo) and a significant decrease in the content of palladium were detected.

In our laboratory, various substances were exposed to incandescent lamps [8] [9]. Release of excess heat and changes in the elemental composition in the substances surrounding the lamp were detected. In one of the experiments, the tube-shaped incandescent lamp was wrapped in a lead-tin alloy ribbon. In order to prevent the alloy from melting, running water was used. Many elements ranging from lithium to bismuth were reliably detected.

It is important to note the following. Many attempts to explain LENR include hydrogen or deuterium as a necessary element of the process. In the lead-tin alloy ribbon experiment, nuclear transmutations occur in the complete absence of

hydrogen. This indicates the need for approaches to explain LENR that do not require the mandatory presence of hydrogen.

Many nickel-hydrogen reactors have been tested in our laboratory [10]. In some of them, elemental and isotopic composition of both the nickel-hydrogen core and the surrounding matter was analyzed. Many initially absent elements were always detected, not only in the core, but also in the surrounding matter.

One of our reactors (M7) ran continuously for 7 months, generating up to 1000 watts of excess power [11]. Figure 1 and Figure 2 show what new elements appeared in different parts of the reactor after the end of its operation. New elements (K, Ca, V, Cr, Ti, Mn, Fe, Zn, Ga, Sr, Ba, Yb, Hf) appeared in all parts of the reactor located near the core, even in the outer ceramic tube. Analysis was made of the isotopic composition of nickel, which, along with hydrogen, was considered as "fuel". Contrary to expectations, even after a long stay in a working reactor, it almost did not change. The isotopic composition of nickel remained

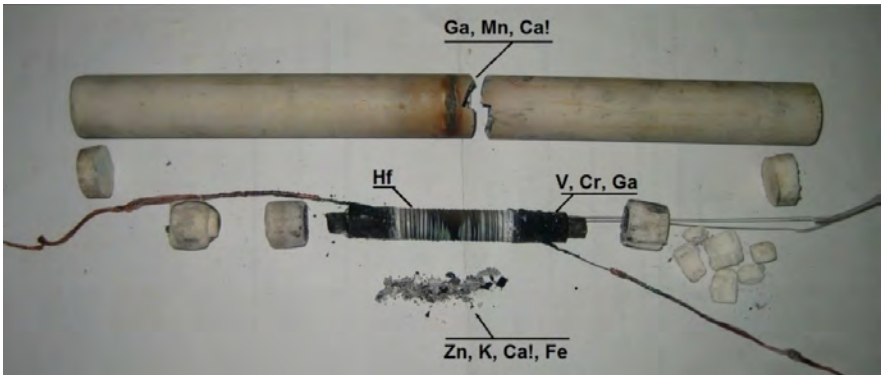

Figure 1. M7 reactor after shutdown. Many elements that had been initially all but absent in the fuel were found in the fuel and in the reactor structure and calcium in especially significant quantities. In the inner ceramic tube the calcium content reached 23% with an initial content of about 1%.

Figure 2. Cross section of M7 reactor inner tube.

almost unchanged in our other nickel-hydrogen reactors. This indicates that LENR processes (heat generation, transmutations) occur not so much in the hot nickel-hydrogen core, but in surrounding matter.

3. Important features of LENR

Numerous diverse experiments allow us to highlight a number of important features of LENR:

1) huge variety of nuclides appears not only in the "fuel", but also in surrounding matter, and, in general, nuclides that do not have radioactivity appear;

2) energy is released far beyond the capabilities of chemical reactions;

3) neutrons and gamma radiation are emitted during the LENR process. However, the radiation intensity is many orders of magnitude lower than in "normal" nuclear reactions;

4) a dense medium (solid, liquid, dense plasma) is required;

5) unusual tracks appear near the reactors.

4. Attempts to Explain the LENR Phenomenon

Many attempts have been made to explain the LENR phenomenon. Numerous hypotheses can be divided into several groups:

- proton (deuteron) overcomes the "Coulomb barrier" and merges with the nucleus;
- proton turns into a neutron, for which there is no "coulomb barrier". This neutron generates a chain of nuclear transformations;
- LENR processes involve a catalyst;
- An atom enters a compact state with the release of high energy. In addition, an atom in a compact state overcomes the "Coulomb barrier" more easily.

But so far, it has not been possible to explain all the features of LENR, or at least some of them without contradicting the rest. Basically, the search went in the direction of finding ways to overcome the "Coulomb barrier", which prevents a sufficiently close approach of the nuclei. An example of this approach is the well-known Widom-Larsen theory [12], which allows possibility of converting protons into neutrons. Resulting neutrons react with the nuclei of surrounding matter, forming new chemical elements. However, in reality, experiments did not detect the intense radiation of neutrons and hard gamma rays, which inevitably occur when neutrons are captured by nuclei. This alone refutes this type of hypothesis. Similar inconsistencies are typical for other approaches. It should be emphasized that none of the above approaches provide an explanation for the huge variety of nuclides that arise.

5. Assumption of Energy-Efficient Rearrangements of Nucleons Located in More Atoms

The problem of the appearance of huge variety of emerging nuclides can be solved by the assumption that they appear as a result of energy-efficient rear-

rangements of nucleons located in two or more atoms [13] [14]. To do this, they must be exposed to action that covers several atoms at the same time. Indeed, if one assumes the multi-nucleated nature of the transformations, the appearance of numerous diverse nuclides becomes possible. Papers [15] [16] describe results of computer calculations of the simplest variant of multicore transformations: exothermic transformations of one or two stable nucleons into one or two stable nucleons with or without the participation of electrons. A computer calculation revealed more than a million variants in this simplest type of multicore transformation.

Possible nuclear transformations in corundum (Al_2O_3) are shown below as an example. Corundum is substance that has been widely used in our reactors. Even when considering the interactions of only two aluminum nuclei, many new helium-to-iron nuclides can arise:

$^{27}Al + {}^{27}Al \rightarrow {}^{54}Fe + 21.242$ MeV $^{27}Al + {}^{27}Al \rightarrow {}^{50}Cr + {}^{4}He + 13.428$ MeV

$^{27}Al + {}^{27}Al \rightarrow {}^{42}Ca + {}^{12}C + 4.137$ MeV $^{27}Al + {}^{27}Al \rightarrow {}^{38}Ar + {}^{16}O + 5.058$ MeV

$^{27}Al + {}^{27}Al \rightarrow {}^{34}S + {}^{20}Ne + 5.058$ MeV $^{27}Al + {}^{27}Al \rightarrow {}^{30}Si + {}^{24}Mg + 3.971$ MeV

$^{27}Al + {}^{27}Al \rightarrow {}^{29}Si + {}^{25}Mg + 0.688$ MeV $^{27}Al + {}^{27}Al \rightarrow {}^{28}Si + {}^{26}Mg + 3.308$ MeV

Additional nuclides can arise from interactions of two oxygen nuclei and nuclei of oxygen and aluminum:

$^{16}O + {}^{16}O \rightarrow {}^{32}S + 16.539$ MeV $^{16}O + {}^{16}O \rightarrow {}^{31}P + {}^{1}H + 7.673$ MeV

$^{16}O + {}^{16}O \rightarrow {}^{28}Si + {}^{4}He + 9.594$ MeV $^{16}O + {}^{27}Al \rightarrow {}^{42}Ca + {}^{1}H + 9.312$ MeV

$^{16}O + {}^{27}Al \rightarrow {}^{39}K + {}^{4}He + 9.438$ MeV $^{16}O + {}^{27}Al \rightarrow {}^{31}P + {}^{12}C + 2.502$ MeV

Thus, in corundum H, He, C, O, Ne, S, Ar, Mg, Si, P, Ca, Cr, Fe may appear. Many of these new elements were discovered by analyzing the corundum tubes that worked in our reactors.

It should be noted that such transformations cannot occur through the channel of strong interactions due to the "Coulomb barrier". But nothing prevents, in principle, such transformations from occurring through the channel of weak nuclear interactions. In this case, a neutrino or antineutrino must be present in the equations of nuclear reactions.

It is important to note that transformations involving an ensemble of a large number of nuclei occur mainly without the formation of the radioactive nuclides and excited nuclei that cause gamma radiation. This is due to the fact that in a system of a large number of interacting nuclei, there are many options for the formation of products with stable and unstable isotopes, with excited and unexcited nuclei. In accordance with the Ziegler principle, a non-equilibrium system develops in such a way as to maximize entropy production under given external constraints [17]. Entropy production in the formation of stable and unexcited nuclides is higher than in the formation of unstable and excited ones, so their formation is more likely.

As already mentioned, for the implementation of multi-core interactions, a mechanism covering several atoms is necessary. Here are a few hypothetical

ways to implement multinucleated transformations:

- Magnetic monopoles [4] [5] [17] [18] [19] [20] [21];
- "Capsules" with transatoms [22];
- Magneto-toro-electric clusters [23];
- High density Charge Clusters [24];
- Ultra-low-energy neutrinos [8] [25].

Let us consider the last of the listed approaches, as it allows one without contradiction to explain the main features of LENR and without involving "new entities" devoid of experimental confirmation.

6. Hypothesis of Low-Energy Neutrinos Participation in Nuclear Transformations

Theoretical works on the interaction of neutrinos with matter at very low energies give an extremely low probability of interaction [26] [27]. But a number of experiments indicate that, in fact, neutrinos at low energies interact with matter quite noticeably [28] [29].

It is important to note that approaches mastered by high-energy neutrino physics are unsuitable for very low-energy neutrinos (of the order of 1 eV and below). The difference in energy is about the same as between that of gamma quanta and light photons. Photons manifest themselves in a completely different and much more diverse way than gamma quanta. Apparently, neutrinos at very low energies also have many important but unexplored properties. But something is quite clear. The large de Broglie wavelength, which is many times greater than the interatomic distances, leads to the fact that the interaction covers a huge number of atoms. Of very low energy neutrinos interact with matter macroscopically, *i.e.* they are refracted, reflected at the boundaries of media, scattered on inhomogeneities. Streams of such neutrinos experience interference and diffraction. In these processes, there is practically no energy exchange between neutrinos and matter.

In addition, neutrinos work in nuclear transformations involving the weak interaction. Unlike other types of interactions, the role of the weak nuclear interaction is not in attraction or repulsion, but in the transformation of neutrons into protons or protons into neutrons with the participation of electrons or positrons and antineutrinos and neutrinos. At the same time, in addition to fulfilling the laws of conservation of energy, momentum, angular momentum, baryon and electric charge, the lepton charge must be preserved. Neutrinos or antineutrinos act as a kind of key that resolves nuclear reactions of weak interaction. In addition, they can contribute additional energy. For example, the well-known nuclear reaction $\tilde{\nu} + p \rightarrow e^+ + n$ is possible when the neutrino energy is greater than 1806 keV. But if the energy balance of the nuclear conversion is positive, no additional energy is required, only the presence of neutrinos. For example, the reverse beta decay of $\nu + {}^{60}Co \rightarrow {}^{60}Ni + e^- + 2.823$ MeV can occur at an arbitrarily low neutrino energy. However, such nuclei have spontaneous beta radioactivity,

therefore this reaction must be observed against the background of spontaneous decays. A noticeable effect can be at a sufficiently high neutrino flux density. This is achieved, for example, in the focus of a parabolic mirror in which a small beta source is located [28] [29]. When scanning the celestial sphere, bursts of ^{60}Co activity were observed, many times exceeding the background of spontaneous radioactivity (sometimes by 1000 times). It is assumed that the increase in the decay rate of the beta source is caused by concentrated flows of very low-energy neutrinos—the dark matter component.

As noted above, a lot of nuclear transformations are, in principle, possible when two or more nuclei are converted into two or more other nuclei with a positive energy balance [8] [15] [16]. The Coulomb barrier does not allow the nuclei to get close enough for the strong nuclear interaction to work. But in the presence of a neutrino that "includes" the weak interaction covering both nuclei, nothing prevents the reactions from occurring, for example:

$$\nu + {}^{27}\mathrm{Al} + {}^{27}\mathrm{Al} + e^- \rightarrow {}^{53}\mathrm{Cr} + {}^{1}\mathrm{H} + 13.594\ \mathrm{MeV}$$

$$\nu + {}^{27}\mathrm{Al} + {}^{27}\mathrm{Al} \rightarrow {}^{50}\mathrm{Cr} + {}^{4}\mathrm{He} + 13.428\ \mathrm{MeV} + \nu'$$

The neutrino on the left side of the equations can have an arbitrarily low energy. The neutrino on the right side of the second equation has a high energy and flies away, carrying away a significant part of the released energy.

Currently, there is no exact data on the rest mass of the electron neutrino (antineutrino). Direct experiments show that it is less than 0.8 eV [30]. Estimates based on astronomical observations give a mass value less than 0.28 eV [31]. Studies of neutrino oscillations indicate a neutrino mass value less than 0.05 eV [32]. If it is true that the mass of an electron neutrino and an antineutrino is so small, then neutrino-antineutrino pairs can be formed as a result of inelastic collisions of particles of matter (electrons, ions, neutral atoms) during their thermal motion. The energy of colliding particles must be more than twice the mass of the particles being born. **Figure 3** shows the fraction of particles of matter with thermal motion energy greater than 0.1 and 0.5 eV at temperatures up to 10000˚C [8] [25]. It can be seen that the formation of neutrino-antineutrino pairs is possible in matter at a temperature above a threshold, which depends on the mass of neutrinos and antineutrinos (about 100˚C if the mass is 0.05 eV and about 1000˚C if the mass is 0.25 eV). Note that the production of excess heat in nickel-hydrogen LENR reactors requires heating to a temperature of at least 1100˚C [10] [11].

Especially often, electrons collide with atoms in metals: in 1 cm^3, there are about 10^{36} collisions per second [8] [25]. Such a high frequency of collisions leads to the appearance of huge number of neutrinos and antineutrinos, even with a very small probability of their formation. Resulting neutrinos and antineutrinos can interact with the nuclei of surrounding matter. In addition, neutrinos and antineutrinos can appear from light photons, since their energy is sufficient to form a pair of neutrinos-antineutrinos.

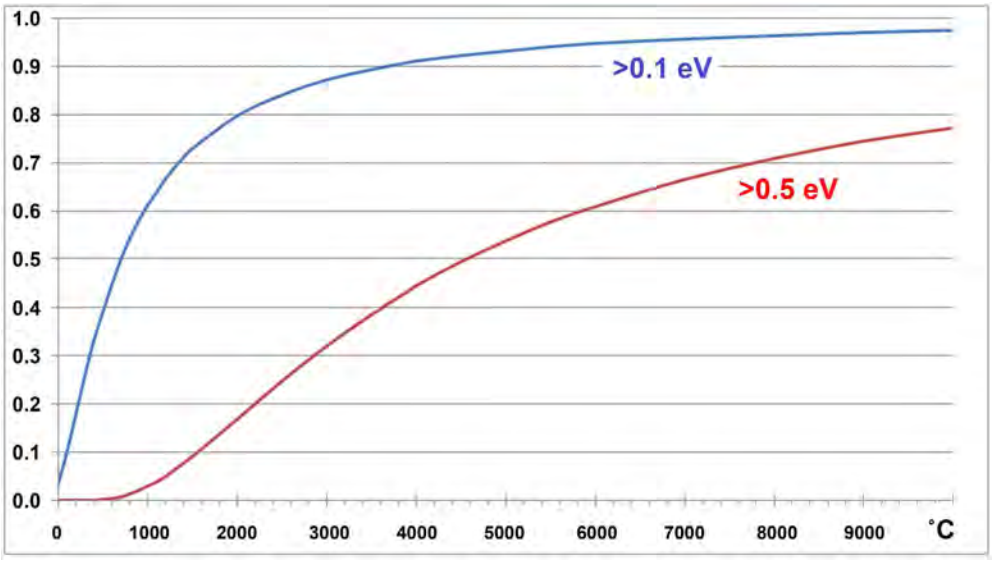

Figure 3. Fraction of matter particles with a thermal motion energy greater than 0.1 and 0.5 eV.

It is important to note that de Broglie wavelength $\lambda = h/p$ (h: Planck constant, p: momentum) of emerging neutrinos and antineutrinos is about 1 micron. This means that region of interaction covers a huge number of atoms, and this makes transformations involving many atoms and nuclei possible, as a result of which even unlikely processes become significant [28] [29] [33].

Figure 4 shows dependence of the de Broglie wavelength, *i.e.*, the size of the interaction region, on neutrino or antineutrino energy. It can be seen that at energies of the order of 10 keV and higher, only one nucleus can be covered by the interaction. At energies of several keV, the interaction already covers several atoms. And neutrinos and antineutrinos, which arise from thermal collisions of atoms of matter with an energy of less than 1 eV, cover many billions of atoms by their interaction.

Here are some examples of possible nuclear transformations of two nuclei, electron and neutrino or antineutrino. In nickel and in nickel with participation of hydrogen, iron, cobalt, copper, and helium may appear:

$$\nu^{-} + {}^{58}\mathrm{Ni} + {}^{61}\mathrm{Ni} + e^{-} \rightarrow {}^{63}\mathrm{Cu} + {}^{56}\mathrm{Fe} + 1.736\ \mathrm{MeV}$$
$$\nu^{-} + {}^{58}\mathrm{Ni} + {}^{64}\mathrm{Ni} + e^{-} \rightarrow {}^{65}\mathrm{Cu} + {}^{57}\mathrm{Fe} + 0.113\ \mathrm{MeV}$$

$$\nu^{-} + {}^{58}\mathrm{Ni} + {}^{61}\mathrm{Ni} + e^{-} \rightarrow {}^{59}\mathrm{Co} + {}^{60}\mathrm{Ni} + 2.252\ \mathrm{MeV}$$
$$\nu^{-} + {}^{60}\mathrm{Ni} + {}^{61}\mathrm{Ni} + e^{-} \rightarrow {}^{59}\mathrm{Co} + {}^{62}\mathrm{Ni} + 0.276\ \mathrm{MeV}$$

$$\nu + {}^{61}\mathrm{Ni} + {}^{64}\mathrm{Ni} \rightarrow {}^{65}\mathrm{Cu} + {}^{60}\mathrm{Ni} + e^{-} + 0.409\ \mathrm{MeV}$$
$$\nu + {}^{61}\mathrm{Ni} + {}^{64}\mathrm{Ni} \rightarrow {}^{63}\mathrm{Cu} + {}^{62}\mathrm{Ni} + e^{-} + 0.995\ \mathrm{MeV}$$

$$\nu^{-} + {}^{60}\mathrm{Ni} + {}^{1}\mathrm{H} + e^{-} \rightarrow {}^{61}\mathrm{Ni} + 7.041\ \mathrm{MeV}$$
$$\nu^{-} + {}^{61}\mathrm{Ni} + {}^{1}\mathrm{H} + e^{-} \rightarrow {}^{62}\mathrm{Ni} + 9.808\ \mathrm{MeV}$$

$$\nu^{-} + {}^{60}\mathrm{Ni} + {}^{1}\mathrm{H} + e^{-} \rightarrow {}^{4}\mathrm{He} + {}^{57}\mathrm{Fe} + 0.569\ \mathrm{MeV}$$
$$\nu^{-} + {}^{61}\mathrm{Ni} + {}^{1}\mathrm{H} + e^{-} \rightarrow {}^{4}\mathrm{He} + {}^{58}\mathrm{Fe} + 2.794\ \mathrm{MeV}$$

$$\nu + {}^{61}\mathrm{Ni} + {}^{1}\mathrm{H} \rightarrow {}^{4}\mathrm{He} + {}^{58}\mathrm{Ni} + e^{-} + 0.865\ \mathrm{MeV}$$
$$\nu + {}^{64}\mathrm{Ni} + {}^{1}\mathrm{H} \rightarrow {}^{4}\mathrm{He} + {}^{61}\mathrm{Ni} + e^{-} + 1.98\ \mathrm{MeV}$$

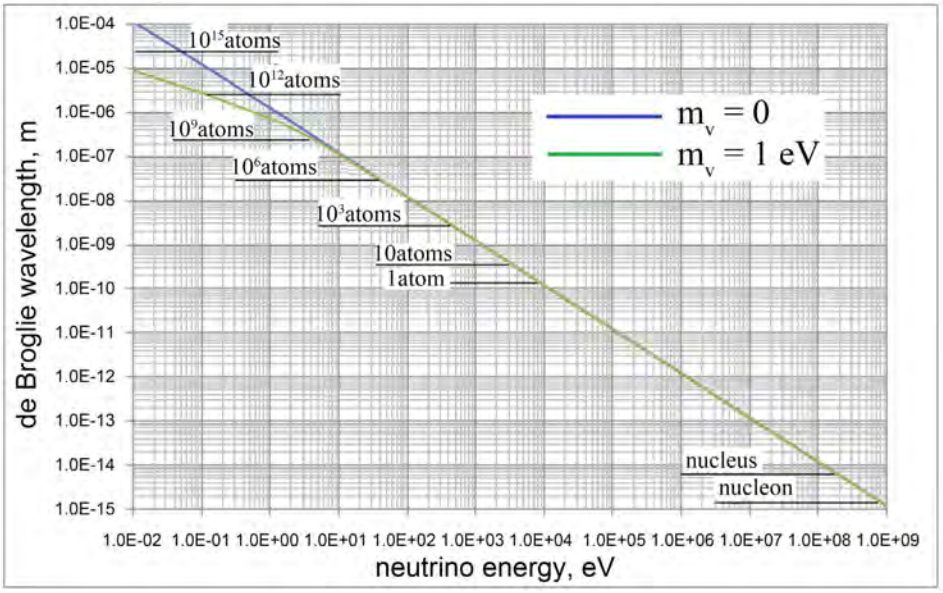

Figure 4. Dependence of de Broglie wavelength of neutrino or antineutrino (size of the interaction region) on the neutrino energy. Indicates how many atoms of solid or liquid matter are in the neutrino interaction region at a given energy.

Indeed, iron, cobalt and copper were found as impurities in nickel-hydrogen reactors that had been operated.

Appearance of iron from water in the Energoniva reactor [3] becomes clear. Combination of the nucleons contained in three water molecules and four electrons gives the iron nucleus:

$$4\nu^{-} + 3H_2O + 4e^{-} \rightarrow {}^{54}Fe_{26} + 87.81 \text{ MeV}$$

Finally, it is possible to explain the paradoxical phenomenon discovered by Louis Kervran [34]: in the absence of calcium in chicken feed, hens managed to produce calcium from potassium:

$${}^{39}K_{19} + {}^{1}H_1 \rightarrow {}^{40}Ca_{20} + 8.337 \text{ MeV}$$

This transformation cannot occur through strong interaction channel due to "Coulomb barrier". And if it could, huge release of energy in this nuclear reaction would have incinerated the animal.

However, if the same transformation goes through the channel of weak interactions involving neutrinos, both of these problems are solved:

$$\nu + {}^{39}K_{19} + {}^{1}H_1 \rightarrow {}^{40}Ca_{20} + \nu' + 8.337 \text{ MeV}$$

Triggering this transformation low energy neutrinos can be generated during cellular metabolism. As a result of the nuclear reaction, two particles arise: calcium nuclei and neutrinos. Since in a system of two particles, energy is distributed inversely to mass, almost all the energy is carried away by neutrino, without leaving it in the chicken.

7. Conclusions

Unlike many other hypotheses, hypothesis of low-energy neutrinos participation

in nuclear transformations allows us to explain many features of LENR:

- the appearance of a large variety of nuclides not only in "fuel", but also in surrounding matter;
- the need to heat or give matter particles energy in another way;
- the need for a sufficiently dense environment;
- no (or very low intensity) of hard nuclear radiation.

It is important to note that there is no "Coulomb barrier problem" in nuclear transformations involving neutrinos.

Acknowledgements

Authors would like to thank T. Timerbulatov, S. Zabavin and I. Stepanov for supporting the research and helping with equipment; R. Karabanov and I. Kamputin for high-quality analysis of chemical composition; N. Samsonenko, L. Urutskoev, A. Chistolinov and V. Vysotskiy for helpful discussions and valuable criticism; I. Savvatimova, A. Klimov, V. Zatelepin, R. Grinyer V. Zhigalov, G. Levi, A. Prosvirnov, S. Godin, V. Panchelyuga, A. Kovacs and many other people in Russia and abroad for their support and valuable advice.

Conflicts of Interest

The authors declare no conflicts of interest regarding the publication of this paper.

References

[1] Karabut, A.B., Kucherov, Y.R. and Savvatimova, I.B. (1992) *Physics Letters A*, **170**, 265-276. https://doi.org/10.1016/0375-9601(92)90252-H

[2] Savvatimova, I.B. (2011) *Journal of Condensed Matter Nuclear Science*, **8**, 1-19.

[3] Vachaev, A.V., Ivanov, N.I., Ivanov, A.N. and Pavlova, G.A. (1994) Method of Obtaining Elements and Device for Its Implementation. Patent of the Russian Federation No. 2096846, MKI G 21 G 1/00, H 05 H 1/24.

[4] Urutskoev, L.I., Liksonov, V.I. and Tsinoev, V.G. (2002) *Annales de la Fondation Louis de Broglie*, **27**, 701-726.

[5] Ivoilov, N.G. (2006) *Annales de la Fondation Louis de Broglie*, **31**, 115-123.

[6] Mastromatteo, U. (2016) *Journal of Condensed Matter Nuclear Science*, **19**, 173-182.

[7] Biberian, J.-P. (2020) Transmutation Induced by Laser Irradiation. Le colloque RNBE 2020. 21 November.

[8] Parkhomov, A.G. and Karabanov, R.V. (2021) *RENSIT*, **13**, 45-58. https://doi.org/10.17725/rensit.2021.13.045

[9] Parkhomov, A.G. and Karabanov, R.V. (2021) *Journal of Forming Areas of Science*, **27**, 116-119. http://www.unconv-science.org/pdf/27/parkhomov2.pdf

[10] Parkhomov, A.G., Alabin, K.A., Andreev, S.N., *et al.* (2017) *RENSIT*, **9**, 74-93. https://doi.org/10.17725/rensit.2017.09.074

[11] Parkhomov, A.G., Zhigalov, V.A., Zabavin, S.N, *et al.* (2019) *Journal of Forming Areas of Science*, **23**-**24**, 57-63. http://www.unconv-science.org/pdf/23/parkhomov2.pdf

[12] Widom, A. and Larsen, L. (2006) *The European Physical Journal C*, **46**, 107-111.

[13] Kuznetsov, V., Mishinsky, G., Penkov, F., Arbuzov, V. and Zhemenik, V. (2003) *Annales de la Fondation Louis de Broglie*, **28**, 173-213.

[14] Filippov, D.V. and Urutskoev, L.I. (2004) *Annales de la Fondation Louis de Broglie*, **29**, 1187-1206.

[15] Parkhomov, A.G. (2017) *Journal of Forming Areas of Science*, **17**-**18**, 99-101.

[16] Parkhomov, A.G. (2018) *International Journal of Unconventional Science*, **E3**, 32-33. http://www.unconv-science.org/pdf/e3/parkhomov-en.pdf

[17] Martyushev, L.M. and Seleznev, V.D. (2006) *Physics Reports*, **426**, 1-45. https://doi.org/10.1016/j.physrep.2005.12.001

[18] Lochak, G. (1985) *IJTP*, **24**, 1019-1050. https://doi.org/10.1007/BF00670815

[19] Fredericks, K.A. (2013) *Engineering Physics*, **6**, 15-45.

[20] Daviau, C., Fargue, D., Priem, D. and Racineux, G. (2013) *Annales de la Fondation Louis de Broglie*, **38**, 139-153.

[21] Kovacs, A. (2020) Magnetic Monopole Mass and Charge Radius Calculation from Experimental Data Analysis. *Proceedings of the* 26*th Russian Conference on Cold Nuclear Transmutations and Ball Lightning*, Moscow, 28 September-2 October 2020, 205-219.

[22] Mishinsky, G.V. (2017) *RENSIT*, **9**, 147-160. https://doi.org/10.17725/rensit.2017.09.147

[23] Dubovik, V.M., Shishkin, A.L., Baranov, V.A., Vinogradova, A.V. and Tatur, V.Yu. (2012) Investigation of the Characteristics of Magnetotroelectric Radiation Using Photofilm Detectors. http://www.trinitas.ru/rus/doc/0231/004a/02311041.htm

[24] Shoulders, K.R. (1987) EV: A Tale of Discovery. Jupiter Technologies, Austin.

[25] Parkhomov, A.G. (2019) *International Journal of Unconventional Science*, **E4**, 3-5. http://www.unconv-science.org/pdf/23/parkhomov1-en.pdf

[26] Cocco, A.G., Mangano, G. and Messina, M. (2007) *Journal of Cosmology and Astroparticle Physics*, **706**, 15. https://doi.org/10.1088/1475-7516/2007/06/015

[27] Lazauskas, R., Vogel, P. and Volpe, C. (2007) Charged Current Cross Section for Massive Cosmological Neutrinos Impinging on Radioactive Nuclei. https://doi.org/10.1088/0954-3899/35/2/025001

[28] Parkhomov, A.G. (2018) *Journal of Modern Physics*, **9**, 1617-1632. https://doi.org/10.4236/jmp.2018.98101

[29] Parkhomov, A.G. (2019) Space. Earth. Human. New Views on Science. 251 p. https://www.amazon.com/dp/171122121X

[30] KATRIN Collaboration (2022) *Nature Physics*, **18**, 160-166. https://doi.org/10.1038/s41567-021-01463-1

[31] Thomas, S.A., Abdalla, F.B. and Lahav, O. (2010) *Physical Review Letters*, **105**, Article ID: 03130. https://doi.org/10.1103/PhysRevLett.105.031301

[32] Kajita, T. (2015, December 8) Discovery of Atmospheric Neutrino Oscillations. Nobel Lecture. https://www.nobelprize.org/uploads/2018/06/kajita-lecture.pdf

[33] Aharonov, Y. and Avignore, F.T. (1987) *Physical Review Letters*, **58**, 1173-1175. https://doi.org/10.1103/PhysRevLett.58.1173

[34] Kervran, L. (1998) Biological Transmutations. Happiness Press, Magalia.

Journal of Modern Physics, 2022, 13, 285-300
https://www.scirp.org/journal/jmp
ISSN Online: 2153-120X
ISSN Print: 2153-1196

Non Ideal Schottky Barrier Diode's Parameters Extraction and Materials Identification from Dark *I-V-T* Characteristics

M. Bashahu, D. Ngendabanyikwa, P. Nyandwi

Department of Physics and Technology, Institute of Applied Pedagogy, Bujumbura, Burundi
Email: bashahuma@yahoo.fr

How to cite this paper: Bashahu, M., Ngendabanyikwa, D. and Nyandwi, P. (2022) Non Ideal Schottky Barrier Diode's Parameters Extraction and Materials Identification from Dark *I-V-T* Characteristics. *Journal of Modern Physics*, **13**, 285-300.
https://doi.org/10.4236/jmp.2022.133020

Received: December 8, 2021
Accepted: March 6, 2022
Published: March 9, 2022

Abstract

Several parameters of a commercial Si-based Schottky barrier diode (SBD) with unknown metal material and semiconductor-type have been investigated in this work from dark forward and reverse *I-V* characteristics in the temperature (*T*) range of [274.5 K - 366.5 K]. Those parameters include the reverse saturation current (I_s), the ideality factor (n), the series and the shunt resistances (R_s and R_{sh}), the effective and the zero bias barrier heights (Φ_B and Φ_{B0}), the product of the electrical active area (A) and the effective Richardson constant (A^{**}), the built-in potential (V_{bi}), together with the semiconductor doping concentration (N_A or N_D). Some of them have been extracted by using two or three different methods. The main features of each approach have been clearly stated. From one parameter to another, results have been discussed in terms of structure performance, comparison on one another when extracted from different methods, accordance or discordance with data from other works, and parameter's temperature or voltage dependence. A comparison of results on Φ_B, Φ_{B0}, n and N_A or N_D parameters with some available data in literature for the same parameters, has especially led to clear propositions on the identity of the analyzed SBD's metal and semiconductor-type.

Keywords

SBD, Dark Forward and Reverse *I-V-T* Characteristics, Different Parameters Extraction Methods, Identification of the Structure's Metal and Semiconductor-Type

1. Introduction

Rectifying metal-semiconductor (MS) contacts, also known as Schottky barrier diodes (SBDs), have received an increasing attention due to their applications in

photovoltaic solar cells [1] [2] [3] [4], field effect transistors (FETs) [5], infrared high-speed detectors, electronic switching and other high-frequency devices [6] [7] [8] [9]. Many reports on SBDs physical properties have been proposed in order to better understand the performance of those structures and related devices. The four SBD's key parameters are the reverse saturation current (I_s), the ideality factor (n), the series resistance (R_s) and the effective Schottky barrier height (SBH, Φ_B) [10]. Together with the SBH at zero bias (or the asymptotic SBH) (Φ_{B0}), the electrical active area (A), the effective Richardson constant (A^{**}) and the semiconductor doping concentration (N_A or N_D), those parameters can be extracted by using different methods based on current-voltage (I-V) characteristics [11]-[28]. Besides this first group of methods, capacitance-voltage (C-V) techniques are used to extract majority carrier concentration (N_A or N_D), activation energy (E_A), densities (n_{is}) and energy levels (E_{is}) of interface states. In addition, photo-response measurements, which involve various spectroscopic techniques, are implemented in order to extract parameters such as band-gap, impurity and doping concentration, layer thickness, surface roughness and texture [29] [30]. Methods from those three groups are combined in some reports [4] [31]-[37].

While several methods from those groups are analytical ones, numerical techniques are also used [1] [2] [9] [38] [39] [40] [41] [42]. Moreover, as shown in some review reports [43] [44] [45] [46], from one method to another, two or several parameters can be simultaneously extracted; dc or ac, static or dynamic, fixed or varying frequency and temperature operation's conditions can be applied; different current transport mechanisms may be taken into account; results can be temperature or voltage dependent; and they may be compared one another when different methods are combined.

The SBD analyzed in this work is a commercial Si-based one from ST Microelectronics, for which neither the metal nor the semiconductor-type (p- or n-) were specified in the relevant catalog. By using dark forward and reverse current-voltage (I-V) characteristics at different temperatures, together with different approaches, our objective was three-fold: firstly to extract different parameters of that structure, secondly to discuss our results, and thirdly to especially come to identify the SBD's metal and semiconductor-type.

2. Experimental Details

The SBD sample of this analysis is shown magnified in **Figure 1** and has the following actual specifications: blue color, BAT 48 as trade mark, diameter and length of the central part equal to 0.15 cm and 0.3 cm, respectively, diameter and length of each of the two terminal's wires equal to 0.7 mm and 3.0 cm, respectively.

Reverse and forward I-V-T characteristics of the diode were measured in dark conditions over bias voltage and temperature ranges of [−2.5; +0.5] V and [274.5; 336.5] K, respectively. A common experimental arrangement of simple equipments

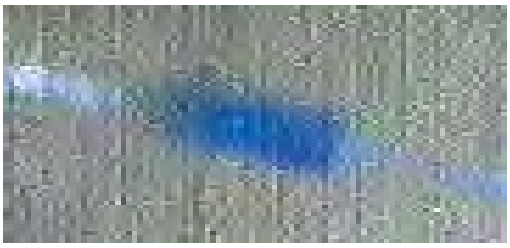

Figure 1. Magnified view of the SBD of this study.

has been used for that purpose. These include notably a power supply with d.c emf fixed to a maximum value E_0 = 2.5 V; a rheostat mounted with the power supply in such a way to vary the emf, an ammeter and a voltmeter for *I-V* measurements; an ice bath and an electrical heater to change thermal conditions of the sample, and a thermometer for temperature measurements.

3. Extracted Parameters, Used Methods, Results and Discussion

3.1. R_{sh} from Reverse *I-V* Plots

The complete representation of a real diode's *I-V* characteristic is given by Equation (1) [47]:

$$I = I_s\left\{\exp\left[\frac{q(V-R_sI)}{nK_BT}\right]-1\right\}+\frac{V-R_sI}{R_{sh}} \quad (1)$$

where I_s, n, R_s and R_{sh} are the diode's reverse saturation current, ideality factor, series resistance and shunt resistance, respectively, while q is the absolute value of the electronic charge and K_B is the Boltzmann's constant. The first term of the sum in Equation (1) represents the diode current and the second term describes the current through the shunt resistance (I_p). The simplest way to extract R_{sh} or the related shunt conductance (G_p) consists in determining the slope of the straight line representing the reverse *I-V* characteristic. That slope is given by Equation (2) [48]:

$$G_p = \frac{1}{R_{sh}} = \frac{\Delta I_p}{\Delta V} \quad (2)$$

For the considered temperature range, the obtained SBD's reverse *I-V* lines (**Figure 2** is the plot of such a line at T = 286.5 K) were so merged that they have led to an almost constant shunt resistance: $R_{sh} = (4.93 \pm 0.07) \times 10^4\ \Omega$. This has been a proof of the scarcity of crystal irregularities or defects in the bulk and at the edges of our SBD, through which current losses could occur.

3.2. I_s, R_s and n from Forward lnI_d-V Plots

With the assumption of thermoionic emission (TE) as the prevailing charge transport mechanism in the SBD, the forward diode's *I-V* characteristic is given by [19] [47] [49]

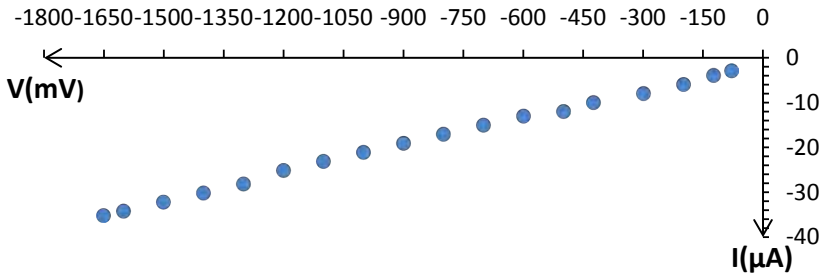

Figure 2. Plot of reverse *I-V* data for the SBD at 286.5 K.

$$I_d = I_s\left[\exp\left(\frac{qV}{nK_BT}\right)-1\right] \tag{3}$$

In Equation (3), the reverse saturation current (I_s) is expressed as

$$I_s = AA^{**}\left(\frac{-\Phi_B}{K_BT}\right) \tag{4}$$

where T is the diode's absolute temperature, A is the junction's electrically active area, A^{**} is the effective Richardson constant and Φ_B is the effective Schottky barrier height (SBH). When the forward bias $V > \frac{3K_BT}{q}$, Equation (3) is given by [50]

$$I_d = I_s\exp\left(\frac{qV}{nK_BT}\right) \tag{5}$$

According to Equation (5), n and I_s parameters can be, respectively, extracted from the slope and the intercept of the linear region (diffusion line) in the plot of the experimental $\ln I_d$- V data. Nevertheless, the presence of a parasitic series resistance affects the I-V characteristic mostly at high voltages. To account for this, Equation (5) is re-arranged to become

$$I_d = I_s\exp\left[\frac{q(V-R_sI)}{nK_BT}\right] \tag{6}$$

Using Equation (6) and following the Cowley and Sze method (ref. no. 2 in [43]), one extracts R_s from the gap ΔV (on the V-axis) between the actual $\ln I_d$ vs V curve and the diffusion line. **Figure 3** is the plot of that curve for our SBD at one fixed temperature. On that plot, as different R_s are obtained at different I_d in the related region, a mean R_s-value is extracted.

Values of n, I_s and R_s determined according to the previous methodology are summarized in **Figure 4**.

$n(T)$ data from **Figure 4** exhibit a somehow wavy trend, while results from other works state a slight decrease of the ideality factor with increasing temperature [19] [22] [36] [51]. Nevertheless, values of n for our SBD are higher than those commonly observed for c-Si solar cells [44]. Moreover, the ideality factor of our sample has values in good agreement with those of other investigated Si-based SBDs, e.g.: $1.2 < n < 2.7$ for Pt/p-Si [16].

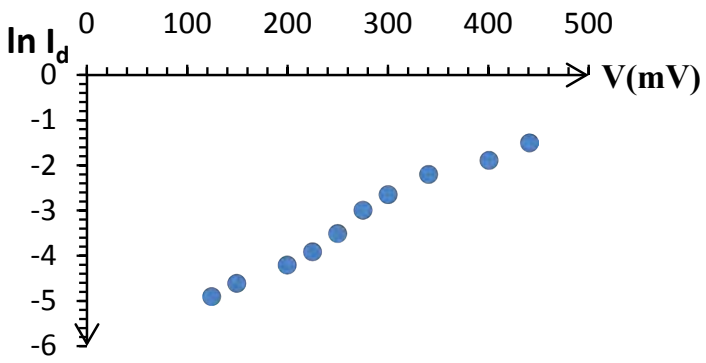

Figure 3. Plot of $\ln I_d$- V data for the SBD of this study at T = 317 K.

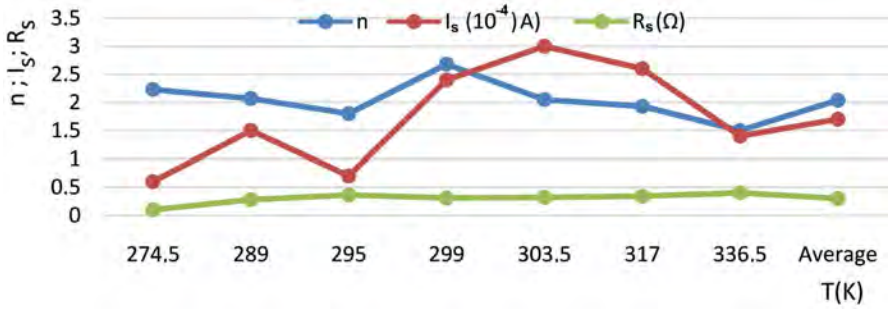

Figure 4. Plots of n, I_s and R_s vs T data for the SBD of this study.

The average series resistance (R_s) of our SBD is much higher than R_s-values commonly observed for c-Si solar cells [43]. This is likely due to high resistivity (ρ) of Si-based SBDs (e.g.: ρ is equal to 15 Ω cm for Tb/p-Si; 8 Ω cm for Ru/n-Si and 1 Ω cm for Pt/n-Si) [52], compared to resistivity of p-Si and n-Si materials (and thus of p-n Si junctions). As examples, ρ lies in the ranges [4×10^{-4}; 3×10^{-2}] Ω cm and [10^{-4}; 6×10^{-2}] Ω cm for n-Si and p-Si, respectively, when the doping concentration decreases from 10^{+21} cm^{-3} to 10^{+18} cm^{-3} [6].

At its side, the reverse saturation current (I_s) may increase with increasing temperature according to Equation (4). That theoretical trend is not well evidenced by results of **Figure 4**. Nevertheless, those results do not depart too much from I_s-values observed elsewhere for some Si-based SBDs in the same temperature and voltage ranges. As examples, I_s is equal to 7×10^{-5} A for a Cr Si_2/n-Si junction at 300 K and for $V \in$ [0.12; 0.35] V [53], and to 4×10^{-4} A for an epitaxial $CoSi_2$/n-Si diode with an area of 0.61 mm^2, at 292 K and $V \in$ [0.2; 0.5] V [51].

3.3. Φ_B and AA^{**} from the Activation Energy Method

From Equations (4) and (5), assuming $n \approx 1$, the SBD's forward I-V characteristic is expressed as

$$I = AA^{**}T^2 \exp\left[-\left(\frac{\Phi_B - qV}{K_B T}\right)\right] \tag{7}$$

and thus

$$\ln\left(I/T^2\right) = \ln\left(AA^{**}\right) - \left(\frac{\Phi_B - qV}{K_B}\right)\frac{1}{T} \tag{8}$$

The activation energy method is based on the plot of experimental $\ln(I/T^2)$-$(1/T)$ data at a given voltage bias $V > \frac{3K_BT}{q}$. From such an Arrhenius (or Richardson) plot, the effective Schottky barrier height (Φ_B) and the AA^{**} product (of the contact's electrically active area and the effective Richardson constant) can be derived from the negative slope and the intercept of the expected resulting straight line, respectively. Based on experimental forward *I-V-T* data on the SBD of this analysis, results of such a determination are shown in Figure 5.

The SBHs in Figure 5 are estimates of actual Φ_B since too many approximations are used in the present method. Moreover, experimental data points have been found scattered in each $\ln(I/T^2)$-$(1/T)$ plot. Nevertheless, a clear increase of the SBH with increasing bias voltage is noticed in agreement with theory (e.g. in Section 3.4).

The AA^{**} mean product is equal to 2.35×10^{-6} A/K^2. Using that result and the effective Richardson constants of 12 and 32×10^4 A·m^{-2}·K^{-2} for n-Si and p-Si, respectively [6] [52], one finds the contact's electrically active area A of the SBD equal to 2.23 μm^2 and 7.81 μm^2 for n-Si and p-Si, respectively. Those values correspond to diameters of 1.69 μm and 3.15 μm, respectively, which are clearly lower than the measured diameter (=0.7 mm) of each terminal's wire.

3.4. Φ_{B0} from the SBH's Bias Dependence Behavior

The basic equation used to estimate the SBH within the TE theory is obtained by combining Equations (3) and (4):

$$I_d = AA^{**}T^2 \exp\left(\frac{-\Phi_B}{K_BT}\right)\left[\exp\left(\frac{qV}{K_BT}\right) - 1\right] \tag{9}$$

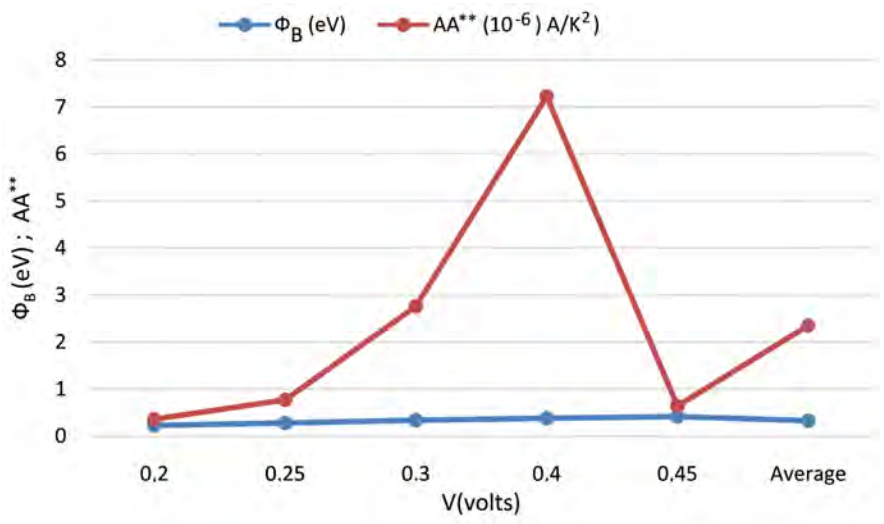

Figure 5. Results of Φ_B and AA^{**} obtained from Richardson's plots.

As the SBH is strongly dependent on the electrical field in the depletion region and thus on the applied bias, Φ_B is commonly expressed as [16] [19]

$$\Phi_B = \Phi_{B0} + \beta V \tag{10}$$

where Φ_{B0} is the barrier height at zero bias (or the asymptotic barrier height) and β is assumed to be a positive constant over the region of measurement. That means an increase of the SBH with increasing bias voltage. This trend is experimentally observed from results in **Figure 5**. If the ideality factor in defined as in Equation (11)

$$\frac{1}{n} = 1 - \beta \tag{11}$$

then the forward *I*-*V* characteristic of Equation (9) becomes:

$$I_d = I_0 \exp\left(\frac{qV}{nK_BT}\right)\left[1 - \exp\left(\frac{-qV}{K_BT}\right)\right] \tag{12}$$

where

$$I_d = AA^{**}T^2 \exp\left(\frac{-\Phi_{B0}}{K_BT}\right) \tag{13}$$

For bias voltage $V > \frac{3K_BT}{q}$, Equation (12) reduces in the following simple form

$$I_d \approx I_0 \exp\left(\frac{qV}{nK_BT}\right) \tag{14}$$

From Equation (13), the SBH at zero bias is expressed as:

$$\Phi_{B0} = K_BT \ln\left(AA^{**}T^2/I_0\right) \tag{15}$$

where I_0 is the reverse saturation current extrapolated at zero bias. Equation (15) offers a way to determine Φ_{B0} using AA^{**} data from **Figure 5** and I_s-values from **Figure 4** ($I_0 \approx I_s$ since extrapolated at zero bias). The results of such a determination are shown in **Figure 6**.

In accordance with Equation (10), values of Φ_{B0} are lower than those of Φ_B from **Figure 5**. Nevertheless, Φ_{B0}-T data exhibit a wavy trend whereas results from other works state that the SBH and its value at zero bias slightly increase with increasing temperature [19] [54].

3.5. *n*, R_s and Φ_B from the Auxiliary Cheung's Functions

In this method, firstly Equation (6) (with $I_d = I$) is re-arranged as

$$\ln I = \ln I_s + \frac{qV}{nK_BT} - \frac{qR_sI}{nK_BT} \tag{16}$$

and thus

$$V = \frac{nK_BT}{q}\ln I + R_sI - \frac{nK_BT}{q}\ln I_s \tag{17}$$

Differentiating Equation (17) provides:

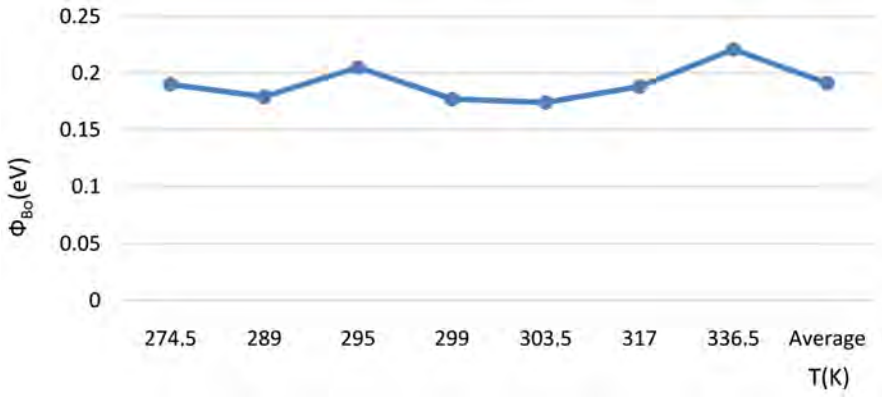

Figure 6. Results of Φ_{B0} vs T data for the SBD of this study.

$$dV = \frac{nK_BT}{q} d(\ln I) + R_s dI \tag{18}$$

and thus

$$\frac{dV}{d(\ln I)} = \frac{nK_BT}{q} R_s I \tag{19}$$

Equation (19) shows that, from experimental forward I-V data at a given temperature, the curve $\left[dV/d(\ln I)\right]$-I is a straight line from which R_s and nK_BT/q can be extracted as the slope and the intercept, respectively.

Secondly, combining Equations (4) and (6) (with $I_d = I$) yields

$$\ln\left(\frac{I}{AA^{**}T^2}\right) + \frac{\Phi_B}{K_BT} = \frac{q}{K_BnT}V - \frac{q}{K_BnT}R_s I \tag{20}$$

Equation (20) is re-arranged to become

$$H(I) = R_s I + n\Phi_B \tag{21}$$

where

$$H(I) = V - \frac{nK_BT}{q}\ln\left(\frac{I}{AA^{**}T^2}\right) \tag{22}$$

Equations (19), (21) and (22) are the three auxiliary Cheung's functions [14]. Using the AA^{**} mean value of Figure 5 and experimental forward I-V data at a given temperature, allows one to get $H(I)$ data from Equation (22). The plot of those $H(I)$ data (Equation (21)) leads to a straight line from which R_s and $n\Phi_B$ can be extracted as the slope and the intercept, respectively. Figure 7 shows a curve of $[dV/d(\ln I)]$-I data at a fixed temperature. Its points are quite scattered, whereas $H(I)$ data present a good linear behaviour at bias voltages $V > \frac{3K_BT}{q}$ as illustrated in Figure 8.

The values of n, R_s and Φ_B derived by using the previous procedure are presented in Figure 9.

It is shown that values of the ideality factor obtained from $[dV/d(\ln I)]$-I plots (average n = 1.65) are quite lower than those extracted from $\ln I_d$-V plots (in

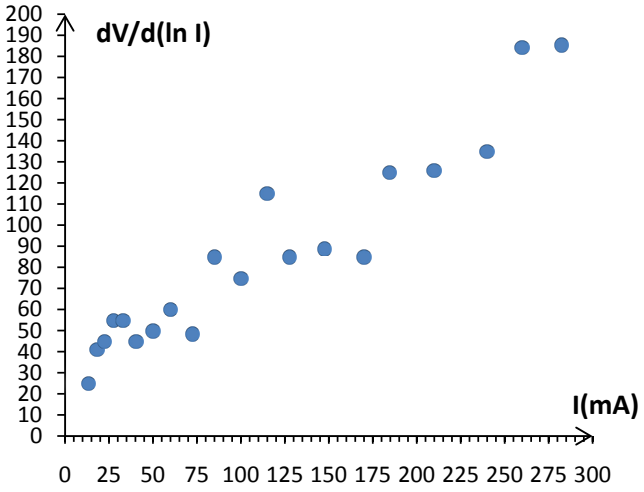

Figure 7. Plot of [d V/d(ln$I$)]-I data for the SBD of this study at T = 295 K.

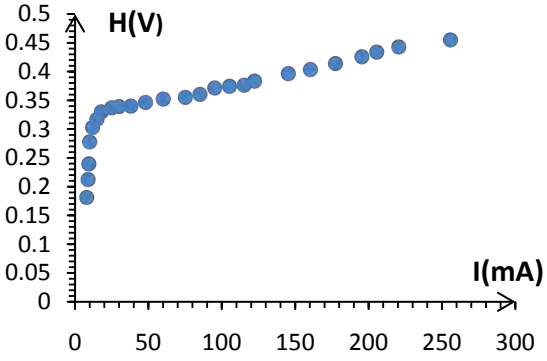

Figure 8. Plot of $H(I)$ data for the SBD of this analysis at T = 299.5 K.

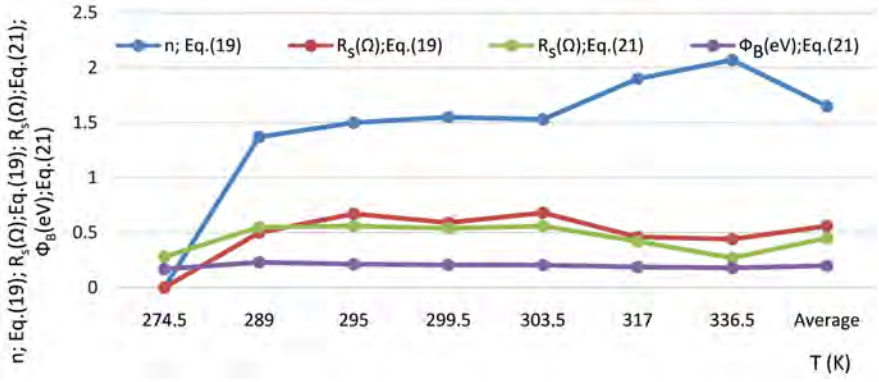

Figure 9. Results of n, R_s and Φ_B extracted from the auxiliary Cheung's functions.

Figure 4, average n = 2.04). Moreover, while $n(T)$ data from Figure 4 show a wavy trend, $n(T)$ results of the present method ([d V/d(lnI)]-I plots) seem to increase with increasing temperature.

A comparison of R_s-results of Figure 4 and Figure 5 shows that [d V/d(lnI)]-I plots yield higher values (mean R_s = 0.56 Ω), followed by data from H-I plots (mean R_S = 0.45 Ω), lnI_d-V plots leading to lower results (mean R_s = 0.30 Ω).

The auxiliary Cheung's functions method leads also to lower SBHs (mean Φ_B = 0.198 eV) than the activation energy method (in **Figure 5**, mean Φ_B = 0.325 eV). Moreover, a mean trend of SBH data from the Cheung's method is a decrease with increasing temperature and with increasing ideality factor. This is in accordance with statements from other works [14] [16] [49] [51].

3.6. V_{bi} from the Maximum Forward Current Method

At a given temperature, the SBD's maximum forward current ($I_d = I_{\max}$) is recorded at bias voltage V equal to the junction's built-in potential (V_{bi}), for which Equation (14) becomes [19]

$$I_{\max} \approx I_0 \exp\left(\frac{qV_{bi}}{nK_BT}\right) \tag{23}$$

or

$$\ln I_{\max} \approx \ln I_0 + \frac{qV_{bi}}{nK_B}\frac{1}{T} \tag{24}$$

Therefore, in the experimental I-V characteristics at different temperatures, accounting only for data corresponding to $I_{\max}$, one gets a plot of $\ln I_{\max}$-$\frac{1}{T}$. On the expected resulting straight line, the V_{bi} and $I_0 \approx I_s$ parameters are extracted from the slope and intercept, respectively. Estimates obtained by using that procedure and n-values of **Figure 9**, for the SBD and temperature range of this analysis, have been: V_{bi} = 0.496 V and $I_s = 0.34 \times 10^{-4}$ A, respectively.

3.7. N_A or N_D from Reverse I-V-T Data

In forward bias conditions, the SBH increases with increasing bias voltage as shown in **Figure 5** (Section 3.3) and Section 3.4. At the opposite, in reverse bias case, the main effect is the lowering of the SBH with the applied bias voltage $|V|$. In that case, the reverse current is expressed as [19]

$$I_R = I_0 \exp\left[\frac{q}{K_BT}\left(\frac{qE}{4\pi\varepsilon_s}\right)^{1/2}\right] \tag{25}$$

where I_0 is the reverse current at zero bias and the E quantity is given by

$$E = \left[\frac{2qN}{\varepsilon_s}\left(|V| + V_{bi} - \frac{K_BT}{q}\right)\right]^{1/2} \tag{26}$$

with ε_s the semiconductor's dielectric constant. If $V_{eff} = |V| + V_{bi} \gg \frac{K_BT}{q}$, then Equation (25) becomes

$$I_R \approx I_0 \exp\left(\alpha V_{eff}^{1/4}\right) \tag{27}$$

where the α parameter is expressed as

$$\alpha = \frac{q}{K_BT}\left(\frac{q}{4\pi\varepsilon_s}\right)^{1/2}\left(\frac{2qN}{\varepsilon_s}\right)^{1/4} \tag{28}$$

Equation (27) may be also written as

$$\ln I_R \approx \ln I_0 + \alpha V_{eff}^{1/4} \tag{29}$$

According to Equation (29), by using experimental reverse I-V data at a given temperature, together with the V_{bi} -value stated in section 3.6, $\varepsilon_s = 11.9\varepsilon_0$ for Si [19], and $\varepsilon_0 = 8.854\times10^{-12}\ \mathrm{F\cdot m^{-1}}$ [55], one gets a plot of $\ln I_R$-$V_{eff}^{1/4}$ data, which is expected to yield a straight line, and of which $I_0 \approx I_s$ and α (thus $N = N_A$ or N_D) parameters can be extracted from the intercept and the slope, respectively. An example of such a plot is shown in **Figure 10**. The N and $I_0 \approx I_s$ results obtained by following that procedure are given in **Figure 11**.

A comparison of our SBD reverse saturation current's results shows that the reverse I-V-T data method leads to slightly lower values (**Figure 11**, mean I_s = 1.31×10^{-4} A) than those from the forward.

$\ln I_d$-V plots (**Figure 4**, mean I_s = 1.7×10^{-4} A). Moreover, the reverse I-V-T data method appears to be better than the $\ln I_d$-V one for I_s-parameter extraction, since its results clearly exhibit an increase of reverse saturation current with increasing temperature, in accordance with theory.

Furthermore, for the SBD and the temperature range of this analysis, the semiconductor (Si)'s average doping concentration is found equal to 6.06×10^{18}

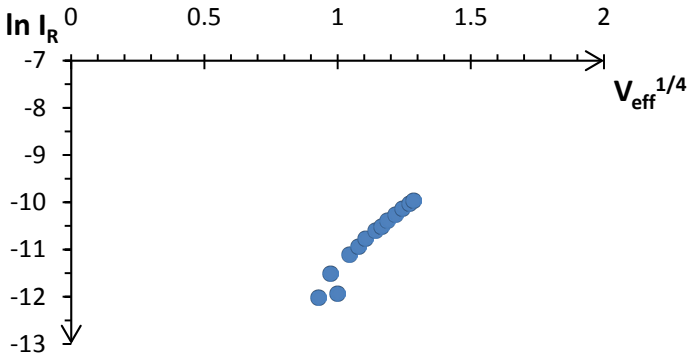

Figure 10. Plot of $\ln I_R$ vs $V_{eff}^{1/4}$ data points for the SBD of this study at T = 299.

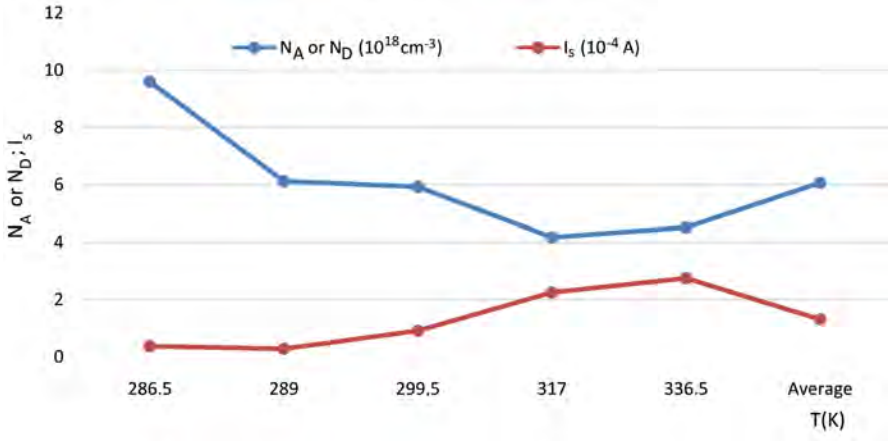

Figure 11. Results of N_A or N_D and I_s obtained from reverse I-V-T data.

Table 1. Synthesis of the obtained results and the used methods for SBD's parameters extraction in this analysis.

N°	Parameter	mean value	Extraction method	Comments
1	R_{sh}	$(4.93 \pm 0.07) \times 10^4\ \Omega$	Slope of reverse I-V plots	Not temperature dependent
2	n	2.04	$\ln I_d$- V plots	Temperature (T) dependent
		1.65	$[\mathrm{d}V/\mathrm{d}(\ln I)]$-$I$ plots	Increases with increasing T
3	R_s	0.30 Ω	$\ln I_d$- V plots	Increases with increasing T
		0.56 Ω	$[\mathrm{d}V/\mathrm{d}(\ln I)]$-$I$ plots	Temperature dependent
		0.45 Ω	Cheung's H-I plots	Temperature dependent
4	I_s	1.7×10^{-4} A	$\ln I_d$- V Plots	Increases with increasing T
		0.34×10^{-4} A	$I_{\max}$-$(1/T)$ plots	----
5	Φ_B	0.325 eV	Arrhenius plots	Increases with increasing V
		0.198 eV	Cheung's H-I plots	Decrease with increasing T
6	AA^{**}	2.35×10^{-6} A·K^{-2}	Arrhenius plots	Increases with increasing V
7	Φ_{B0}	0.191 V	V dependence of Φ_B	Temperature dependent
8	V_{bi}	0.496 V	$I_{\max}$-$(1/T)$ plots	----
9	N_A or N_D	$6.06 \times 10^{+18}$ cm^{-3}	Reverse I-V-T data	Decreases with increasing T

cm^{-3}. This indicates that, either n- or p-type, the actual Si material has a resistivity ρ of about 10^{-2} Ω cm [6].

3.8. Results Summary

For the SBD and the temperature range of this analysis, Table 1 shows in synthesis the obtained parameters' mean values and the extraction methods implemented so far.

3.9. Device Materials Identification

On one hand, the following data on some SBDs are reported amongst others in literature: 1) $\Phi_B = (0.272 \pm 0.005)$ eV and $\Phi_{B0} = (0.196 \pm 0.008)$ eV for a typical PtSi/p-Si structure, whereas $\Phi_B \in [0.847; 0.868]$eV for a Pt Si/n-Si diode at room temperature [16]; 2) $\Phi_B = 0.25$ eV for an Au/p-Si (chem.) contact, and $\Phi_B = 0.20$ eV for a PtSi/p-Si (back sputtering) diode from I-V data [6]; 3) $n \in [1.2; 2.7]$ for Pt/p-Si [16]; 4) with a doping concentration of 10^{+18} cm^{-3}, the resistivity, $\rho = 3 \times 10^{-2}$ Ω cm and 6×10^{-2} Ω cm for n-Si and p-Si materials, respectively [6]. On the other hand, the parameters' results obtained for the SBD and the temperature range of this study are presented in Table 1. A comparison of results on the same parameters in those two sets of data, allows one to certify that the SBD of this analysis is either Pt Si/p-Si or Au/p-Si.

4. Conclusion

As shown in the synthesis of Table 1, from I-V-T measurements and the use of different methods, up to nine parameters have been extracted on a Si-based MS

contact with unknown metal and semiconductor-type materials. Two of those parameters, *i.e.* the shunt resistance (R_{sh}) and the semiconductor doping concentration (N_A or N_D), have been derived from reverse *I-V-T* data. All the remaining seven parameters have been determined from forward *I-V-T* data. Those are the ideality factor (n), the series resistance (R_s), the reverse saturation current (I_s), the effective Schottky barrier height (SBH, Φ_B), the SBH at zero bias (Φ_{B0}), the product of the contact's electrical active area (A) and the effective Richardson constant (A^{**}), and the built-in potential (V_{bi}). Some of those seven parameters have been extracted by using two or three different approaches. The main features of each approach, including prevailing current transport mechanism, operation conditions and other assumptions, have been clearly stated. From one parameter to another, results have been discussed in terms of structure performance, parameter's temperature or voltage bias dependence, accordance or discordance with data from other works, and comparison on one another of results obtained from different methods. Furthermore, a comparison of results on the n, Φ_B, Φ_{B0}, and N_A or N_D parameters of Table 1 with some available data on the same parameters in literature, has led to state that the analyzed SBD is either Pt Si/p-Si or Au/p-Si.

Conflicts of Interest

The authors declare no conflicts of interest regarding the publication of this paper.

References

[1] Sellai, A. and Ouennoughi, Z. (2005) *International Journal of Modern Physics C*, **16**, 1043-1050. https://doi.org/10.1142/S0129183105007704

[2] Ku, J., Min, Y., Kim, J., *et al.* (2005) GAAS: Novel SPICE Macro Modeling for an Integrated Si Schottky Barrier Diode. 13*th GAAS Symposium*, Paris, 3-4 October 2005, 409-412.

[3] Tan, Z., Hong, L., Liu, J.-M., *et al.* (2019) *NPG Asia Materials*, **11**, Article No. 20. https://doi.org/10.1038/s41427-019-0120-3

[4] Allen, N.P. (2014) Electrical Characterization of Ruthenium Dioxide Schottky Contacts on Ga N. Thesis (for Master of Sciences in Electrical Engineering), Virginia Polytechnic Institute and State University, Blacksburg.

[5] Pearman, D. (2007) Electrical Characterization and Modeling of Schottky Barrier Metal Source/Drain MOSFETS. PhD Thesis, The University of Warwick, Coventry.

[6] Sze, S.M. (1969) Physics of Semiconductor Devices. Wiley-Interscience, New York, 43, 245, 410-414.

[7] Juang, F.S. and Su, Y.K. (1989) *Solid-State Electronics*, **32**, 661-664. https://doi.org/10.1016/0038-1101(89)90145-7

[8] Malacky, L., Kordos, P. and Novak, J. (1990) *Solid-State Electronics*, **33**, 273-278. https://doi.org/10.1016/0038-1101(90)90166-C

[9] Sarpatwari, K. (2009) Toward Understanding the Electrical Properties of Metal/Semiconductor Schottky Contacts: The Effects of Barrier Inhomogeneities and Geometry in Bulk and Nanoscale Structures. PhD Thesis, The Pennsylvania State

University, The Graduate School, State College.

[10] Mikhelashvili, V.B., Eisenstein, G., Valery, G. and Fainleib, S. (1999) *Journal of Applied Physics*, **85**, 6873-6883. https://doi.org/10.1063/1.370206

[11] Norde, H. (1979) *Journal of Applied Physics*, **50**, 5052-5053. https://doi.org/10.1063/1.325607

[12] Cibils, R.M. and Buitrago, R.H. (1985) *Journal of Applied Physics*, **58**, 1075-1077. https://doi.org/10.1063/1.336222

[13] Sato, K. and Yasumura, Y. (1985) *Journal of Applied Physics*, **58**, 3655-3657. https://doi.org/10.1063/1.335750

[14] Cheung, S.K. and Cheung, N.W. (1986) *Applied Physics Letters*, **49**, 85-87. https://doi.org/10.1063/1.97359

[15] Bohlin, K.E. (1986) *Journal of Applied Physics*, **60**, 1223-1224. https://doi.org/10.1063/1.337372

[16] Chin, V.W.L., Storey, J.W.V. and Green, M. (1989) *Solid-State Electronics*, **32**, 475-478. https://doi.org/10.1016/0038-1101(89)90029-4

[17] Osvald, J. and Dobrocka, E. (1996) *Semiconductor Science and Technology*, **11**, 1198. https://doi.org/10.1088/0268-1242/11/8/014

[18] Mikhelashvili, V.B., Eisenstein, G. and Uzdin, R. (2001) *Solid-State Electronics*, **45**, 143-148. https://doi.org/10.1016/S0038-1101(00)00227-6

[19] Safak, H., Sahin, M. and Yüksel, O.F. (2002) *Solid-State-Electronics*, **46**, 49-52. https://doi.org/10.1016/S0038-1101(01)00273-8

[20] Bouzidi, K., Chegear, M. and Aillerie, M. (2012) *Energy Procedia*, **18**, 1601-1610. https://doi.org/10.1016/j.egypro.2012.06.001

[21] Karboyan, S., Tartarin, J.-G. and Lambert, B. (2013) Analysis of Barrier Inhomogeneities in AlGaN/GaN HEMTs' Schottky Diodes by I-V-T Measurements. EuMC, Oct. 2013, Nuremberg, Germany. 4 p. hal-01343345.

[22] Jyotti, I., Yang, H.-D., Choi, C.J., *et al.* (2013) *Materials Transactions*, **54**, 1655-1660. https://doi.org/10.2320/matertrans.M2013015

[23] Liu, Y., Tang, W.M. and Lai, P.T. (2016) *Physica Status Solidi* (*a*), **213**, 2764-2768. https://doi.org/10.1002/pssa.201600110

[24] Mayimele, M.A., Auret, F.D., Janse van Rensburg, J.P. and Diale, M. (2016) Analysis of Temperature-Dependent Current-Voltage Characteristics and Extraction of Series Resistance in Pd/ZnO Schottky Barrier Diodes. https://doi.org/10.1016/j.physb.2015.07.034

[25] Ghizlane, T., Hassan, O., Abdelkader, B. and Omar, B. (2018) *Periodicals of Engineering and Natural Sciences*, **6**, 331-337. https://doi.org/10.21533/pen.v6i2.535

[26] Sadoon, A. and Kemerchou, I. (2020) *International Journal of Energetica*, **5**, 31-37. https://doi.org/10.47238/ijeca.v5i1.120

[27] Wong, C.P.Y., Troadec, C., Wee, A.T.S. and Goh, K.E.J. (2020) *Physical Review Applied*, **14**, Article ID: 054027. https://doi.org/10.1103/PhysRevApplied.14.054027

[28] Lee, J.I., Brini, J. and Dimitriadis, C.A. (1998) *Electronics Letters*, **34**, 1268-1269. https://doi.org/10.1049/el:19980831

[29] NREL (2006) Measurements & Characterization: Electro-Optical Characterization. National Renewable Energy Laboratory, National Center for Photovoltaics, Middlewest Research Institute, Battele, Golden, NREL/BR-520-40121.

[30] Devi, V.L., Jyothi, I., Reddy, V.R. and Choi, C.-J. (2012) *The Open Applied Physics Journal*, **5**, 1-9. https://doi.org/10.2174/1874183501205010001

[31] Broom, R.F., Meier, H.P. and Walter, W. (1986) *Journal of Applied Physics*, **60**, 1832-1833. https://doi.org/10.1063/1.337226

[32] Cova, P. and Singh, A. (1990) *Solid-State Electronics*, **33**, 11-19. https://doi.org/10.1016/0038-1101(90)90003-W

[33] Chin, V.W.L., Green, M. and Storey, J.W.V. (1990) *Solid-State Electronics*, **33**, 299-308. https://doi.org/10.1016/0038-1101(90)90170-J

[34] Clifford, J.P., Johnson, K.W., Levina, L. and Sargent, E.H. (2007) *Applied Physics Letters*, **91**, Article ID: 253113. https://doi.org/10.1063/1.2823582

[35] Singh, A., Cova, P. and Masut, R.A. (2011) Parameter Extraction from Reverse I-V and C-V Characteristics in an Epitaxial p-InP/Au Schottky Diode. Volume 318, Cambridge University Press, MRS Online Library (OPL), Cambridge. https://doi.org/10.1557/PROC-318-135

[36] Kudryk, Y.Y., Shynkarenko, V.V., Kudryk, R.Y., *et al.* (2014) *Semiconductor Physics, Quantum Electronics & Optoelectronics*, **17**, 398-402. https://doi.org/10.15407/spqeo17.04.398

[37] An, Y., Behnam, A., Pop, E. and Ural, A. (2015) *Journal of Applied Physics*, **118**, Article ID: 114307. https://doi.org/10.1063/1.4931142

[38] Ali, M.H., Rabhi, A., Haddad, S. and El Hajjaji, A. (2017) *Journal of Electronic Materials*, **46**, 6535-6543. https://www.researchgate.net/publication/318690056

[39] Lakehal, B. and Dendouga, A. (2018) *Journal of Nano- and Electronic Physics*, **10**, Article ID: 06046. https://doi.org/10.21272/jnep.10(6).06046

[40] Jang, J.T., Min, J., Kim, D.M., *et al.* (2019) SPICE Compact Model of IGZO Memristor Based on Non-Quasi-Statistically Updated Schottky Barrier Height. *Proceedings of the* 19*th IEEE International Conference on Nanotechnology*, Macau, 22-26 July 2019, 562-565. https://doi.org/10.1109/NANO46743.2019.8993957

[41] Garoudja, E., Falali, W., Oussalah, S., Sengouga, N. and Henini, M. (2020) *Journal of Semiconductors*, **41**, Article ID: 102401. https://doi.org/10.1088/1674-4926/41/10/102401

[42] Liu, X., Zhang, Y., Jin, Z., *et al.* (2021) *Electronics*, **10**, 1540. https://doi.org/10.3390/electronics10131540

[43] Bashahu, M. and Habyarimana, A. (1995) *Renewable Energy*, **6**, 129-138. https://doi.org/10.1016/0960-1481(94)E0021-V

[44] Bashahu, M. and Nkundabakura, P. (2007) *Solar Energy*, **81**, 856-863. https://doi.org/10.1016/j.solener.2006.11.002

[45] Cotfas, D.T., Cotfas, P.A. and Kaplanis, S. (2013) *Renewable and Sustainable Energy Reviews*, **28**, 588-596. https://doi.org/10.1016/j.rser.2013.08.017

[46] Cotfas, D.T., Cotfas, P.A. and Kaplanis, S. (2016) *Renewable and Sustainable Energy Reviews*, **61**, 213-221. https://doi.org/10.1016/j.rser.2016.03.051

[47] Ferhat-Hamida, A., Ouennoughi, Z., Hoffmann, A. and Weiss, R. (2002) *Solid-State Electronics*, **46**, 615-619. https://doi.org/10.1016/S0038-1101(01)00337-9

[48] Araujo, G.L., Sanchez, E. and Marti, M. (1982) *Solar Cells*, **5**, 199-204. https://doi.org/10.1016/0379-6787(82)90027-8

[49] Lee, H.-Y. and Lee, C.-T. (2003) *Solid-State Electronics*, **47**, 831-834. https://doi.org/10.1016/S0038-1101(02)00372-6

[50] Liang, G., Cui, T. and Varahramyan, K. (2003) *Solid-State Electronics*, **47**, 691-694. https://doi.org/10.1016/S0038-1101(02)00324-6

[51] Zhu, S., Detavernier, C., Li, B.-Z., *et al.* (2000) *Solid-State Electronics*, **44**, 1807-1818.

https://doi.org/10.1016/S0038-1101(00)00127-1

[52] Donoval, D., De Sousa Pires, J., Tove, P.A. and Harman, R. (1989) *Solid-State Electronics*, **32**, 961-964. https://doi.org/10.1016/0038-1101(89)90156-1

[53] Aniltürk, Ö.S. and Turan, R. (2000) *Solid-State Electronics*, **44**, 41-48. https://doi.org/10.1016/S0038-1101(99)00204-X

[54] Pristavu, G., Brezeanu, G., Pribeanu, A., *et al.* (2017) *Materials Science Forum*, **897**, 606-609. https://doi.org/10.4028/www.scientific.net/MSF.897.606

[55] Levinshtein, M., *et al.* (1996) Appendices: 1. Basic Physical Constants. In: Levinshtein, M., Rumyantsev, S. and Shur, M., Eds., *Handbook Series on Semiconductor Parameters*, Volume 1, World Scientific Publishing Co. Pte. Ltd., Singapore, 214. https://doi.org/10.1142/9789812832078_bmatter

Journal of Modern Physics, 2022, 13, 301-314
https://www.scirp.org/journal/jmp
ISSN Online: 2153-120X
ISSN Print: 2153-1196

Heuristic Solution to the Conundrum of the *Zitterbewegung*

Juan A. Miranda-Colón

Independent Researcher, Puerto Rico, USA
Email: maruca397@yahoo.com

How to cite this paper: Miranda-Colón, J.A. (2022) Heuristic Solution to the Conundrum of the *Zitterbewegung*. *Journal of Modern Physics*, **13**, 301-314.
https://doi.org/10.4236/jmp.2022.133021

Received: October 12, 2021
Accepted: March 6, 2022
Published: March 9, 2022

Abstract

Assuming the Dirac wavefunction describes the state of a single particle. We propose that the relation derived by Schrödinger, which contains the *Zitterbewegung* term, is a position equation for an amplitude modulated wave. Namely, the elementary constituents are amplitude modulated waves. Indeed, we surmise that a second wave is associated with the particle, which corresponds to a signal. At the same time, we interpret that Broglie's wave corresponds to a carrier. Furthermore, the quantum object is a recording medium and, like in a hologram, information encoded on its surface. We suggest a description and the cause of the *Zitterbewegung* heretofore never considered regarding the previous assertions. Hereunder, we shall also apply the quantum amplitude modulation interpretation to the single-photon wave function by Bialynicki-Birula. The predictions are testable, thence providing evidence for the proposed hypothesis.

Keywords

Zitterbewegung, Electron, Photon, Photon Wave Function, Maxwell's Equations, Measurement Problem

1. Introduction

Per the analysis by Schrödinger of the position operator regarding Dirac's relativistic formalism [1], the free particle, along with its translational motion, ought to exhibit an oscillatory activity that he called the *Zitterbewegung* [2]. The prediction is a high-frequency oscillation at the speed of light in a vacuum with amplitude half the reduced Compton wavelength. The *Zitterbewegung* has been the subject of many studies and discussed in detail in numerous books and papers [3]-[10]. However, after almost a hundred years, it remains an elusive enigma, because there is no consensus on or knowledge of its cause or description and

technological constraints. Its comprehension is paramount, because it is a consequence of the theory at the foundations of quantum electrodynamics.

Some researchers have proposed models that eliminate the "problem" of the *Zitterbewegung*. In contrast, other researchers allege they have observed the *Zitterbewegung* indirectly, simulated by trapped-ion experiments [11] and in a Bose-Einstein condensate [12]. However, the accepted interpretation explains that the *Zitterbewegung* is due to the interference of positive and negative energy plane waves. For the reason that when applying the Foldy-Wouthuysen [13] transformation to wave packets of entirely positive or negative plane waves, there is no *Zitterbewegung* term. Moreover, in quantum electrodynamics, the Dirac wave function does not describe just the state of an electron, but it also contains a part relating to the positron. Indeed, the positive and negative plane waves are interpreted or replaced by a particle-antiparticle annihilating pair, and when the function describing the electron is separated, the *Zitterbewegung* disappears.

Nonetheless, with a fundamental relation between sine and exponential functions, manipulating the *Zitterbewegung* term in the position equation resembles the mathematical representation of amplitude-modulated waves. Therefore, suggesting quantum objects described by Dirac's relativistic formalism are amplitude modulated waves and, the Dirac wave function represents a single entity. There is amplitude modulation interference among the wave packet's positive and negative waves. The positive and negative waves are analogous to a signal and carrier wave. The elementary constituent is a system of two interfering undulations, and the particle is an emergent phenomenon.

A novel interpretation of the quantum theory follows naturally from the Dirac theory, the amplitude modulation hypothesis. At our present technological height, we modulate waves to convey information. Consequently, the quantum object is an information carrier encrypted on its surface. The amount of data is one bit, reminding us of John Archibald Wheeler's famous phrase "it from bit". The mechanism that encrypts information on the surface is the *Zitterbewegung*, an epiphenomenon interpreted here as the expansion and contraction of the elementary constituent [14]. Therefore, regarding the formalism of the Dirac equation, it is our impression that it describes the encoding and transfer of information through a communication channel. This channel is the vacuum or any other medium.

The *Zitterbewegung* for massless quantum objects like photons defers from those with rest mass. Nevertheless, we interpret the proposed wave function for the photon by Bialynicki-Birula amongst others [15] [16] regarding the amplitude modulation interpretation. Consequently, we suggest testable predictions about the photon, illustrating the photon's *Zitterbewegung* and introducing the correct matrices that encode Maxwell's equations in a Dirac-Schrödinger type equation.

2. Quantum Amplitude Modulation

Dirac was not content regarding the Klein-Gordon equation. He sought to ob-

tain a Schrödinger type relativistic wave equation that was first order in time and always gave a positive probabilistic density compared to the Klein-Gordon equation. To achieve his quest, he needed the square root of the relativistic energy-momentum expression. In the subsequent, p represents the momentum, c is the speed of light in a vacuum, $\mathcal{E}$ the energy, m is the relativistic mass, and m_0 the invariant mass.

$$\mathcal{E}^2 = p^2c^2 + m_0^2c^4 \tag{1}$$

Indeed, Dirac factored the equation above with original ineffable insight and obtained his relativistic Hamiltonian H.

$$H = c\boldsymbol{\alpha}\cdot\boldsymbol{p} + m_0c^2\beta. \tag{2}$$

Thus, as a consequence of the Hamiltonian, the time dependence of the position operator of the free particle, calculated in the Heisenberg representation, is the following velocity, where $\hbar$ is the reduced Planck constant, x the position, t time, and i the imaginary unit.

$$\frac{\mathrm{d}x}{\mathrm{d}t} = \frac{i}{\hbar}\left[\boldsymbol{x}, H\right] = c\boldsymbol{\alpha} = \boldsymbol{u} \tag{3}$$

The above, an element of the Dirac Hamiltonian, is the Dirac velocity $\boldsymbol{u}$, and its constituents are 4×4 matrices that, along with β, are known as the gamma matrices. This result is unorthodox since the matrices' eigenvalues are ±1, implying that the absolute value of the particle's velocity in each spatial direction is c. Furthermore, the velocity is not a constant of motion, and its components do not commute with each other or with the Hamiltonian and the momentum; therefore, they cannot be measured simultaneously [17] [18] [19]. Since the velocity is not a constant of motion, Schrödinger found the acceleration that follows where $\omega = H/\hbar$ is an angular frequency.

$$\dot{\boldsymbol{u}} = -2c\omega i\left(\boldsymbol{\alpha}(0) - cH^{-1}\boldsymbol{p}\right)\mathrm{e}^{-2i\omega t}. \tag{4}$$

Since we interpret the Dirac wavefunction describes the state of a single particle. Notice that in the previous equation, there is a dimensionless operator. We will treat it as a unit vector, thus denoting it by $\boldsymbol{\zeta}$. That is, we shall commence the heuristic analysis by assuming that the *Zitterbewegung* has a coordinate system.

$$\boldsymbol{\zeta} = \left(\boldsymbol{\alpha}(0) - cH^{-1}\boldsymbol{p}\right) \tag{5}$$

From this perspective, expanding the exponential term in Equation (4) illustrates the classical equation of acceleration in simple harmonic motion.

$$\dot{\boldsymbol{u}} = -a\left(\sin(2\omega t) + i\cos(2\omega t)\right)\boldsymbol{\zeta} \tag{6}$$

Because it is a free particle, and again, from the perspective of the coordinate system, the acceleration ($a = 2c\omega$) must be internal, suggesting that it has a substructure, subject to two hook-type forces. These forces are out of phase, opposite, and equal magnitude.

Integrating the acceleration, Schrödinger obtained another equation for Dirac's velocity.

$$\boldsymbol{u} = c^2 H^{-1} \boldsymbol{p} + c\mathrm{e}^{-2i\omega t}\boldsymbol{\zeta} \tag{7}$$

The first term in the previous equation is the velocity of a free particle, and, undeniably, it is a group velocity.

$$\boldsymbol{v} = c^2 H^{-1} \boldsymbol{p}. \tag{8}$$

The expression allows the interpretation of Dirac's velocity as phase velocity since rearranging Equation (7) provides a case of Rayleigh's formula, which relates the phase velocity and the group velocity of a wave packet. Furthermore, Pauli's covariant equation is an alternate way to reach the previous conclusion. Pauli formulated Dirac's Hamiltonian in the following covariant form, where γ^μ is a four-vector, in which the space-part is $c\beta\boldsymbol{\alpha}$, and the time-part is $c\beta$.

$$m_0 c^2 = \gamma^\mu p_\mu \tag{9}$$

By comparing the Pauli covariant equation to the phase velocity definition, we deduce that the four-vector, γ^μ is a phase velocity. Therefore, the dilemma that arises from the eigenvalues of the components of Dirac's velocity, found to be troubling because a particle with mass cannot move at light speed, is resolved since we are dealing with a phase velocity, the interference displaces at the rate of the group velocity, rather than that of the phase velocity. We obtain the harmonic oscillator's speed equation by expanding the second term of Equation (7).

$$\boldsymbol{u} = c\left(\cos(2\omega t) - i\sin(2\omega t)\right)\boldsymbol{\zeta} \tag{10}$$

While the interference displaces at the group velocity rate, there is a superimposed oscillation at the speed of light in the vacuum.

Schrödinger continued the examination by integrating the velocity and obtained the following position equation:

$$\boldsymbol{x}(t) = \boldsymbol{x}(0) + c^2 H^{-1}\boldsymbol{p}t + \frac{1}{2} i\hbar c H^{-1}\left(\mathrm{e}^{-2i\omega t} - 1\right)\boldsymbol{\zeta} \tag{11}$$

The first two terms are the position of a particle moving at the group velocity, and the third term is the *Zitterbewegung*, $\boldsymbol{x}_z(t)$. The maximum amplitude of this harmonic oscillation is half the reduced Compton wavelength ($\lambda_r = c\hbar H^{-1}$). The amplitude is equivalent to the fundamental harmonic of a standing wave. The Compton wavelength is considered a particle property relevant to all material particles [20]. Although obtained by applying energy and momentum principles to photons' scattering by electrons, this length appears in quantum phenomena that do not do with scattering. The accepted significance of the Compton wavelength of a particle is the wavelength of a photon whose energy is identical to that particle's invariant mass. However, it is impossible to understand its role in the *Zitterbewegung* and other quantum phenomena with this definition. We interpret that the *Zitterbewegung* relates with the Compton wavelength regarding the amplitude of the elementary constituent's surface oscillations.

$$\boldsymbol{x}_z(t) = \frac{\lambda_r}{2}\left(\sin(2\omega t) + i\cos(2\omega t)\right)\boldsymbol{\zeta} - i\frac{\lambda_r}{2}\boldsymbol{\zeta}. \tag{12}$$

Equation (12), the expansion of the *Zitterbewegung* term, describes a harmonic motion, or pulsation, which occurs around the "stable" kernel of the particle, represented by the second term, which has the same magnitude as the oscillation. The reduced Compton wavelength represents the maximum radius of the free particle. Hence, the relativistic reduced Compton wavelength is the radius of the particle. From this point of view, this length's persistent occurrence, in quantum results, is comprehensible.

$$\lambda_r \to \frac{\hbar c}{\mathcal{E}} = \frac{\hbar}{m_0 c}\sqrt{1-\frac{v^2}{c^2}} \tag{13}$$

The relativistic reduced Compton wavelength is speed-dependent. Therefore a change in the internal structure accounts for results obtained for electrons in scattering experiments. The outcomes from these experiments, conducted at energies around 29 GeV, restricted the particle size to 10^{-18} m or smaller [21]. Thus, researchers interpreted the observation as indicating that the electron is a point particle. However, the reduced relativistic Compton wavelength at the energy range of the experiment is in that order providing evidence for this hypothesis. Technically the elementary constituent resembles a resonating cavity, whose surface has the behavior of a harmonic oscillator. The previous analysis does not reveal the nature of the interference phenomena we are dealing with; however, with the following relation between exponential functions and sine:

$$\sin(\omega t) = \frac{1}{2i}\left(\mathrm{e}^{i\omega t} - \mathrm{e}^{-i\omega t}\right). \tag{14}$$

The *Zitterbewegung* term takes the form of the mathematical representation of an amplitude-modulated wave.

$$\boldsymbol{x}_z(t) = \lambda_r \sin(\omega t)\mathrm{e}^{-i\omega t}\boldsymbol{\zeta} \tag{15}$$

That suggests that the interference that generates the wave packet is an amplitude modulation. Hence, the particle is the interference of two waves, one equivalent to a signal and the other to a carrier, and the bandwidth frequency is the *Zitterbewegung* frequency. These waves' functions are possible to obtain by rewriting the *Zitterbewegung* term as follows, since, wherein the most straightforward amplitude modulation scheme, the modulating signal is usually a sine function. In the following, the amplitude of the signal and carrier, represented by λ_s and λ_c, respectively, and κ is a proportionality constant such that $\kappa\lambda_s\lambda_c = \lambda_r$.

$$\boldsymbol{x}_z(t) = \kappa\left(\lambda_s \sin(\omega t)\right)\left(\lambda_c \mathrm{e}^{-i\omega t}\right)\boldsymbol{\zeta} \tag{16}$$

The velocity associated with the signal is the group velocity in wave packets. Therefore, the carrier is de Broglie's wave. Since the waves are coherent, the wave parameter equations that associate the wavelength to the speed and frequency f are the following.

$$\lambda_s f = v,\ \ \lambda_c f = u \tag{17}$$

The following are the functions where h is Planck's constant, and the value of

the proportionality constant is, $\kappa = 1/\left(4\pi^2\lambda_r\right)$, given that $\lambda_s\lambda_c = 4\pi^2\lambda_r^2$.

$$y_s(t) = \frac{h}{mu}\sin(\omega t) = \lambda_s \sin(\omega t),\ \ y_c(t) = \frac{h}{mv}\mathrm{e}^{-i\omega t} = \lambda_c \mathrm{e}^{-i\omega t} \tag{18}$$

The signal's quotient is the momentum connected to the phase velocity [22]: subsequently, the quantum object has two linear momentums.

Researchers have proposed that the *Zitterbewegung* is a circulatory motion that generates the spin and other related phenomena. The *Zitterbewegung*, according to Hestenes and Rivas [23] [24], is a helical motion. That is, the displacement of the particle is a helix. Indeed Hestenes suggest that the helical motion causes a rotating electric dipole moment and argues that the observed resonance in electron channeling experiments conducted by Gouanère *et al.* is due to the interaction of the dipole field with the crystal lattice [25]. The dissection of the *Zitterbewegung* term illustrates that it is the combination of four oscillatory movements. The following are the position terms of the oscillatory motions, which, we propose, represent a nutation, precession, self-orbital angular momentum, and the spin in that order.

$$\frac{1}{2}i\hbar c^2 H^{-2}\boldsymbol{p},\ -\frac{1}{2}i\hbar c^2 H^{-2}\mathrm{e}^{-2i\omega t}\boldsymbol{p},\ \frac{1}{2}i\hbar c H^{-1}\mathrm{e}^{-2i\omega t}\boldsymbol{\alpha}(0),\ -\frac{1}{2}i\hbar c H^{-1}\boldsymbol{\alpha}(0) \tag{19}$$

There are two angular momentums for each linear momentum associated with the elementary constituent. The nutation and precession are related to the signal and, the others, to the carrier. The vibrations of these intrinsic angular momentum states are synchronized periodic motions like a clock. Because of frequency differences, particles, such as electrons, do not return to their initial phase after a 360˚ rotation. Indeed, the nutation coupled to the precession and the spin coupled to the self-orbital momentum. The nutation and spin complete a cycle at the particle frequency. The precession and orbital motion at the *Zitterbewegung* frequency explain why the electron returns to its original state only after a 720˚ rotation. The nutation and self-orbital momentum generate oscillating electric dipoles, while the precession, like the spin, should cause another magnetic dipole moment for the electron. One of the electric dipoles is proportional to the de Broglie wavelength and vibrates at the *Zitterbewegung* frequency. At the same time, the other is proportional to the signal wavelength vibrating at the particle frequency. The intrinsic electric dipoles differ from those predicted by some versions of the Standard Model since these do not violate the principle of time-reversal symmetry.

3. Single-Particle Entropy

The modulation of waves accomplishes the transmission of information. In amplitude modulation, the instantaneous fluctuation of the signal amplitude induces modifications in the carrier's amplitude, which in the case at hand, causes the surface of the wave packet to expand and contract. Therefore since the Dirac velocity components are not equal, the oscillation is not in phase in all spatial directions, creating distortions on the surface membrane while maintaining a

constant area. Accordingly, analogous to holograms, information encoded on a surface, in the fluctuation patterns, the maximums, and minimums generated by the *Zitterbewegung*. There is a connection between entropy and the information capacity of a system. With the precise mathematical partition function, it is possible to obtain the entropy S of the system. There is a proposed entropy function for the single-particle [26]. However, applying statistical mechanics to systems with few elements determined by quantum rules is unclear for some researchers. In principle, it might not apply to a single particle [27]. Once more, we shall assume the single-particle has entropy and estimate the information it conveys through a heuristic approach. Thus, we will treat the two-wave system as a classical system since it has the behavior of the harmonic oscillator, subject to two forces with the following magnitude: k represents the surface membrane's stiffness.

$$F = \frac{1}{2}\lambda_r k \tag{20}$$

Because the system's natural frequency is the *Zitterbewegung* frequency, the k constant has the following value:

$$k = \frac{4\hbar c}{\lambda_r^3}. \tag{21}$$

Each wave contributes to the energy of the system; therefore, the maximum potential energy is:

$$\mathcal{E} = \frac{1}{4}k\lambda_r^2. \tag{22}$$

We are dealing with the quantum object's inner workings, of which there is no knowledge. Therefore, suppose the equipartition theorem applies to the system and equates to its energy. We obtain the following relation where κ_B is Boltzmann constant, and T is the absolute temperature on the wave packet membrane;

$$\kappa_B T = \frac{1}{4}k\lambda_r^2. \tag{23}$$

The previous equation associates the temperature and acceleration of the surface and resembles the Fulling-Unruh-Davis effect equation by a π factor.

$$T = \left(\frac{\hbar}{2c\kappa_B}\right)a \tag{24}$$

The temperature fluctuates at the *Zitterbewegung* frequency. The relation above also reveals that surface regions reach temperatures higher than the closest star's interior for a particle like an electron. From introductory thermodynamics, if a surface has a temperature, it radiates; it emits photons; that is, the system loses energy. Nonetheless, the energy of a free particle is a constant of motion. Therefore, the electron has come to equilibrium by emitting and absorbing photons; it has a fluctuating gas of photons surrounding it, thereby illustrating another enigmatic result of the Dirac theory:

$$\frac{\mathrm{d}H}{\mathrm{d}t} = -q\boldsymbol{u}\cdot\boldsymbol{E}. \tag{25}$$

The prior is a power equation, where q represents charge, and $\boldsymbol{E}$ is the electric field strength, indicating the electron's energy and electric field fluctuates. Regarding Equation (23), we obtain the magnitude of a force, which is equivalent to that in relation (20).

$$F = \frac{2}{\lambda_r}\kappa_B T \tag{26}$$

This active force is proportional to the temperature; therefore, it is an entropic force, which is phenomenological and not fundamental. The system's statistical tendency to maximize its entropy generates them. This force is perpendicular to the particle surface, where entropy increases [28].

$$T\mathrm{d}S = F\mathrm{d}x \tag{27}$$

The system's entropy equals Boltzmann's constant by substituting Equation (26) and the *Zitterbewegung* amplitude as the integration limit in this version of the second law of thermodynamics.

$$S = \int \frac{F}{T}\mathrm{d}x = \kappa_B \tag{28}$$

Hence, regarding entropy as information, it is equivalent to one bit; each elementary constituent carries or can encode a binary unit of information.

4. Riemann-Silberstein (R-S) Vectors

The previous analysis corresponds to particles with rest mass. For a massless particle like the photon, the phase velocity equals the group velocity; therefore, Equation (5) equals zero. However, as we shall see, the photon also has a particular "trembling motion" and conveys a binary unit of information. We reach this conclusion by interpreting the consequences of applying the amplitude modulation hypothesis to the single-photon wave function Bialynicki-Birula and other researchers proposed. The following equations represent the (R-S) vectors $\boldsymbol{\Gamma}_1$ and its complex conjugate $\boldsymbol{\Gamma}_1^*$ [29], where $\boldsymbol{B}$ is the magnetic field strength and ε_0 the vacuum permittivity.

$$\boldsymbol{\Gamma}_1 = \sqrt{\frac{\varepsilon_0}{2}}\left(\boldsymbol{E} + ic\boldsymbol{B}\right),\ \boldsymbol{\Gamma}_1^* = \sqrt{\frac{\varepsilon_0}{2}}\left(\boldsymbol{E} - ic\boldsymbol{B}\right) \tag{29}$$

According to Bialynicki-Birula, the functions expressed in monochromatic plane waves reveal that each R-S vector represents the photon in a specific helicity and polarization state. Also, they each have equal energy with opposite signs, and each component evolves independently in the vacuum. Therefore, it is necessary to have both vectors to have a complete description of the photon, forming a six-component wave function $\boldsymbol{I}$.

$$\boldsymbol{I} = \begin{pmatrix} \boldsymbol{\Gamma}_1 \\ \boldsymbol{\Gamma}_1^* \end{pmatrix} \tag{30}$$

where the product is the energy per unit volume stored in a photon,

$$\boldsymbol{I}\cdot\boldsymbol{I}^{\dagger}=\frac{\varepsilon_0}{2}\left(E^2+c^2B^2\right)\begin{pmatrix}1\\1\end{pmatrix}. \tag{31}$$

Namely, the proposed wave function is a superposition of quantum states that propagate independently. We commence the analysis by introducing other complex vectors that, with the previous pair, complete a set of eight elements.

$$\boldsymbol{\Gamma}_2=\sqrt{\frac{\varepsilon_0}{2}}\left(i\boldsymbol{E}-c\boldsymbol{B}\right),\ \boldsymbol{\Gamma}_2^*=\sqrt{\frac{\varepsilon_0}{2}}\left(-i\boldsymbol{E}-c\boldsymbol{B}\right)$$

$$\boldsymbol{\Gamma}_3=\sqrt{\frac{\varepsilon_0}{2}}\left(-\boldsymbol{E}-ic\boldsymbol{B}\right),\ \boldsymbol{\Gamma}_3^*=\sqrt{\frac{\varepsilon_0}{2}}\left(-\boldsymbol{E}+ic\boldsymbol{B}\right)$$

$$\boldsymbol{\Gamma}_4=\sqrt{\frac{\varepsilon_0}{2}}\left(-i\boldsymbol{E}+c\boldsymbol{B}\right),\ \boldsymbol{\Gamma}_4^*=\sqrt{\frac{\varepsilon_0}{2}}\left(i\boldsymbol{E}+c\boldsymbol{B}\right)$$

These complex vectors are associated; thereby, knowing one of them, generating the rest is straightforward.

$$\boldsymbol{\Gamma}_1=i\boldsymbol{\Gamma}_4,\ \boldsymbol{\Gamma}_4=i\boldsymbol{\Gamma}_3,\ \boldsymbol{\Gamma}_3=i\boldsymbol{\Gamma}_2,\ \boldsymbol{\Gamma}_2=i\boldsymbol{\Gamma}_1 \tag{32}$$

$$\boldsymbol{\Gamma}_4^*=i\boldsymbol{\Gamma}_1^*,\ \boldsymbol{\Gamma}_3^*=i\boldsymbol{\Gamma}_4^*,\ \boldsymbol{\Gamma}_2^*=i\boldsymbol{\Gamma}_3^*,\ \boldsymbol{\Gamma}_1^*=i\boldsymbol{\Gamma}_2^* \tag{33}$$

$$\boldsymbol{\Gamma}_1=-\boldsymbol{\Gamma}_3,\ \boldsymbol{\Gamma}_2=-\boldsymbol{\Gamma}_4,\ \boldsymbol{\Gamma}_1^*=-\boldsymbol{\Gamma}_3^*,\ \boldsymbol{\Gamma}_2^*=-\boldsymbol{\Gamma}_4^* \tag{34}$$

$$\boldsymbol{\Gamma}_1+\boldsymbol{\Gamma}_2+\boldsymbol{\Gamma}_3+\boldsymbol{\Gamma}_4=0,\ \boldsymbol{\Gamma}_1^*+\boldsymbol{\Gamma}_2^*+\boldsymbol{\Gamma}_3^*+\boldsymbol{\Gamma}_4^*=0 \tag{35}$$

$$\boldsymbol{\Gamma}_n\cdot\boldsymbol{\Gamma}_n^*=\boldsymbol{\Gamma}_1\cdot\boldsymbol{\Gamma}_1^*=\boldsymbol{\Gamma}_2\cdot\boldsymbol{\Gamma}_2^*=\boldsymbol{\Gamma}_3\cdot\boldsymbol{\Gamma}_3^*=\boldsymbol{\Gamma}_4\cdot\boldsymbol{\Gamma}_4^*=\frac{\varepsilon_0}{2}\left(E^2+c^2B^2\right) \tag{36}$$

Moreover, writing the electric and magnetic field strength regarding the R-S vectors is similar to some quantum mechanics equations.

$$\boldsymbol{E}=\frac{\boldsymbol{\Gamma}_1+\boldsymbol{\Gamma}_1^*}{2}=-\frac{\boldsymbol{\Gamma}_3+\boldsymbol{\Gamma}_3^*}{2},\ \boldsymbol{B}=\frac{\boldsymbol{\Gamma}_2+\boldsymbol{\Gamma}_2^*}{2ic}=-\frac{\boldsymbol{\Gamma}_4+\boldsymbol{\Gamma}_4^*}{2ic}$$

As mentioned before, Bialynicki-Birula, by expressing the first R-S vectors in terms of the orthogonal relations regarding monochromatic electromagnetic plane waves, revealed that each vector represents a photon in a specific polarization and helicity state. Hence, following the same procedure with the new R-S vectors indicates that each represents a photon's particular polarization and helicity state; the formalism predicts eight polarization states. Therefore, four possible wave functions suggest four possible types of photons, where each is in two specific polarization modes. In the following, we introduce other helpful relations among the R-S vectors connected with the orthogonal equations, written in a more general and convenient form, where $\boldsymbol{u}'$ represents the photon's phase velocity.

$$\boldsymbol{E}=-\boldsymbol{u}'\times\boldsymbol{B},\ \boldsymbol{B}=\frac{1}{c^2}\boldsymbol{u}'\times\boldsymbol{E},\ \left\|\boldsymbol{u}'\right\|=c \tag{37}$$

$$\boldsymbol{\Gamma}_1^*=\frac{\boldsymbol{u}'}{c}\times\boldsymbol{\Gamma}_2^*,\ \boldsymbol{\Gamma}_2^*=\frac{\boldsymbol{u}'}{c}\times\boldsymbol{\Gamma}_3^*,\ \boldsymbol{\Gamma}_3^*=\frac{\boldsymbol{u}'}{c}\times\boldsymbol{\Gamma}_4^*,\ \boldsymbol{\Gamma}_4^*=\frac{\boldsymbol{u}'}{c}\times\boldsymbol{\Gamma}_1^* \tag{38}$$

$$\boldsymbol{\Gamma}_1=\frac{\boldsymbol{u}'}{c}\times\boldsymbol{\Gamma}_2,\ \boldsymbol{\Gamma}_2=\frac{\boldsymbol{u}'}{c}\times\boldsymbol{\Gamma}_3,\ \boldsymbol{\Gamma}_3=\frac{\boldsymbol{u}'}{c}\times\boldsymbol{\Gamma}_4,\ \boldsymbol{\Gamma}_4=\frac{\boldsymbol{u}'}{c}\times\boldsymbol{\Gamma}_1 \tag{39}$$

Quantum theory asserts that the wave function contains all information about a system, and this state function evolves according to the Schrödinger equation. Therefore, if the R-S vectors are the photon's wave function, it contains all the information. We thereby have laid the foundation for obtaining information about the photon from the proposed wave function with the previous identities.

5. Photon Energy

The corresponding operator is applied to the wave function to extract the desired physical quantity following the quantum mechanics rules. The same results are obtained, starting with whichever of the R-S vectors. Thus the first R-S vector will serve as the example to derive the photon's energy equations.

$$i\hbar\frac{\partial}{\partial t}\mathbf{\Gamma}_n = H\mathbf{\Gamma}_n \tag{40}$$

with Maxwell's equations in the vacuum, the relations among the R-S vector and the momentum operator p we obtain:

$$\begin{aligned} i\hbar\frac{\partial}{\partial t}\mathbf{\Gamma}_1 &= i\hbar\sqrt{\frac{\varepsilon_0}{2}}\left(\frac{\partial \boldsymbol{E}}{\partial t} + ic\frac{\partial \boldsymbol{B}}{\partial t}\right) \\ &= i\hbar\sqrt{\frac{\varepsilon_0}{2}}\left(c^2\nabla\times\boldsymbol{B} - ic\nabla\times\boldsymbol{E}\right) \\ &= i\hbar c\nabla\times\mathbf{\Gamma}_4 \\ &= -c\boldsymbol{p}\times\left(\frac{\boldsymbol{u}'}{c}\times\mathbf{\Gamma}_1\right) \\ &= \left(\boldsymbol{p}\cdot\boldsymbol{u}'\right)\mathbf{\Gamma}_1 - \left(\boldsymbol{p}\cdot\mathbf{\Gamma}_1\right)\boldsymbol{u}' \end{aligned} \tag{41}$$

The second term in the previous equation is the transversality condition, therefore is equal to zero. The first term is the Dirac Hamiltonian for a massless particle.

$$H = \boldsymbol{u}'\cdot\boldsymbol{p} \tag{42}$$

The phase velocity is a Dirac-type velocity, $u_i' = c\alpha_i'$; its components are the subsequent matrices that comply with the Dirac matrices' algebra.

$$\alpha_i'^2 = 1,\ \alpha_i'\alpha_j' + \alpha_j'\alpha_i' = 0 \tag{43}$$

$$\alpha_1' = \begin{pmatrix} 0 & i & 0 & 0 \\ -i & 0 & 0 & 0 \\ 0 & 0 & 0 & -i \\ 0 & 0 & i & 0 \end{pmatrix},\ \alpha_2' = \begin{pmatrix} 0 & 0 & i & 0 \\ 0 & 0 & 0 & i \\ -i & 0 & 0 & 0 \\ 0 & -i & 0 & 0 \end{pmatrix},\ \alpha_3' = \begin{pmatrix} 0 & 0 & 0 & i \\ 0 & 0 & -i & 0 \\ 0 & i & 0 & 0 \\ -i & 0 & 0 & 0 \end{pmatrix}$$

with the previous matrices, the Dirac-type Hamiltonian (42), when squared, reduces to the photon's energy-momentum equation.

$$\mathcal{E} = cp \tag{44}$$

Furthermore, by following the same procedure for the wave function, however, expressed in terms of plane waves, Planck's energy expression results.

$$\mathcal{E} = \omega\hbar \tag{45}$$

6. Photon *Zitterbewegung*

Following the previous analysis, an elementary constituent whose energy equation is a Dirac type Hamiltonian is amplitude modulated wave. Thus since the phase velocity matrices are 4×4, we propose the quantum system is a pair of coupled waves, or two interfering sub-systems, described by a single eight-component wave function.

$$\boldsymbol{\Psi}_n = \begin{pmatrix} \boldsymbol{\psi}_n \\ \boldsymbol{\psi}_n^* \end{pmatrix}. \tag{46}$$

Each wave has four components; the R-S vectors are three of these.

$$\boldsymbol{\psi}_n = \begin{pmatrix} 0 \\ \boldsymbol{\Gamma}_n \end{pmatrix}, \ \boldsymbol{\psi}_n^* = \begin{pmatrix} 0 \\ \boldsymbol{\Gamma}_n^* \end{pmatrix}. \tag{47}$$

Furthermore, Maxwell's equations in free space take the form of a Schrödinger-Dirac-type equation; this is not new, however, written with the correct matrices.

$$i\hbar \frac{\partial \boldsymbol{\psi}_n}{\partial t} = \boldsymbol{u}' \cdot \boldsymbol{p}\boldsymbol{\psi}_n, \ i\hbar \frac{\partial \boldsymbol{\psi}_n^*}{\partial t} = \boldsymbol{u}' \cdot \boldsymbol{p}\boldsymbol{\psi}_n^* \tag{48}$$

Regarding the proposed wave function, since it is a coupled system and the complex conjugate is not a mere mathematical tool to calculate the probability, we predict that the photon's polarization and helicity oscillate: the possible quantum states alternate. Namely, the quantum system is not in a superposition of states in this interpretation. It is a reversible flipping of polarization caused by a continuous fluctuation of the helicity, continuously oscillating from one polarization to another and constantly oscillating. The vibration is the "trembling motion" or *Zitterbewegung* of the photon. The oscillation frequency between states is the photon's frequency, taking twice this frequency to complete a cycle. This alternation of states is the quintessence of a binary code, reversibility from one to zero—the Dzhanibekov Effect aids in the visualization of the fluctuation.

7. Conclusions

Even though the quantum theory is exceptionally successful, this theory has lingering difficulties which have caused the proposal of numerous interpretations. We suggest a new insight that resolves the controversies. With the Dirac formalism, we build a description of the elementary constituents we interpret, which are amplitude modulated waves. It is astonishing to find a particular modulation type in an equation that results from special relativity. The paradigm is a system of two waves analogous to a carrier and signal; the de Broglie wave corresponds to the carrier. Therefore, the Dirac wave function represents a single particle. Namely, the equation providing the phenomenological description of the modulation process is Dirac's quantum relativistic wave equation, where the interference among the undulations generates a discrete entity. Hence, the particle is an emergent phenomenon, and this assertion clarifies the wave-particle duality.

Half of the quantum object has been absent from the theory or analysis, given the possibility of a second wave associated with the quantum object. This omission is the source of the bizarre paradoxes and counterintuitive results.

Following our analysis concerning the possible objective reality of the *Zitterbewegung*, we propose it is a surface effect for material particles as a consequence of amplitude modulation. The quantum entity is a "stable" configuration whose surface, as mentioned before, has the behavior of a harmonic oscillator. There is no dispersion of the wave packet; it expands and contracts. The oscillation encrypts a binary unit of data on the particle's surface. The surface also has a temperature; this is understandable when considering electromagnetic interactions in the Heisenberg formalism. With the time dependence of the Hamiltonian, we interpret the system's energy as fluctuating; it is emitting and absorbing energy in the form of real photons. Indeed, the link between the power and the electron's electric field suggests a way to manipulate inertia, addressed in a forthcoming paper. The amplitude modulation interpretation has testable consequences for the electron with current technologies: an additional magnetic dipole moment and two electric dipole moments.

We introduced matrices that follow the anticomutation relations of the Gamma matrices, and with these, correctly encode Maxwell's equations in a Schrodinger-Dirac type equation. The matrices are the components of the phase velocity for the photon. We also obtained the photon's energy by introducing new R-S vectors and identities. Regarding the proposed eight-component wave function for the single-photon, under this interpretation of the photon's quantum mechanics, the wave function's modulus is not a probability density but an energy density.

Moreover, we hypothesize that the photon's polarization and helicity states are oscillating. Above all, there is no superposition of quantum states in this interpretation of the quantum theory. There is an oscillation amongst the possible quantum states. It can be seen that this settles the measurement problem, and it is the likely cause of the difference in the correlation factor predictions between classical and quantum theory in the entanglement phenomenon. The Entanglement phenomenon is a form of synchronicity; there are no mysterious connections between quantum particles.

Acknowledgements

This research did not receive any specific grant from funding agencies in the public, commercial, or not-for-profit sectors. The author is grateful to Professor Dr. Dorial Castellanos. Dr. Castellanos asked the author regarding the possibility of a second wave associated with the particle.

Conflicts of Interest

The author declares no conflicts of interest regarding the publication of this paper.

References

[1] Dirac, P. (1928) *Proceedings of the Royal Society A*, **117**, 610. https://doi.org/10.1098/rspa.1928.0023

[2] Schrödinger, E. (1930) Über die Kräftefreie Bewegung in der Relativistischen Quantenmechanik. Sitzungsberichte Akad, Berlin, 418.

[3] Hestenes, D. (1990) *Foundations of Physics*, **20**, 1213-1232. https://doi.org/10.1007/BF01889466

[4] Huang, K. (1952) *American Journal of Physics*, **20**, 479-484. https://doi.org/10.1119/1.1933296

[5] Jehle, H. (1971) *Physical Review D*, **3**, 306-345. https://doi.org/10.1103/PhysRevD.3.306

[6] Perkins, G.A. (1976) *Foundations of Physics*, **6**, 237-248. https://doi.org/10.1007/BF00708963

[7] Lock, J.A. (1979) *American Journal of Physics*, **47**, 797-802. https://doi.org/10.1119/1.11697

[8] Robles, P. (2016) *International Journal of Engineering and Technology Research*, **4**, 125-132.

[9] Wang, Z. and Xiong, C. (2006) Zitterbewegung at the Level of Quantum Field Theory.

[10] Sepunaru, D. (2004) *HAIT Journal of Science and Engineering*, **1**, 411-435.

[11] Gerritsma, K., Zähringer, S. and Blatt, R. (2010) *Nature*, **463**, 68-71. https://doi.org/10.1038/nature08688

[12] Leblanc, B., Jimenez-Garcia, P., *et al.* (2013) *New Journal of Physics*, **15**, Article ID: 073011. https://doi.org/10.1088/1367-2630/15/7/073011

[13] Foldy, L. and Wouthuysen, S. (1950) *Physical Review*, **78**, 29-36. https://doi.org/10.1103/PhysRev.78.29

[14] Miranda, J. (1994) Mayagüez (PR). Dissertation/Master's Thesis, University of Puerto Rico, San Juan.

[15] Bialynicki-Birula, I. (1996) The Photon Wave Function. In: Eberly, J.H., Mandel, L. and Wolf, E., Eds., *Coherence and Quantum Optics VII*, Plenum, New York, 313. https://doi.org/10.1007/978-1-4757-9742-8_38

[16] Sipe, J.E. (1995) *Physical Review A*, **52**, 1875. https://doi.org/10.1103/PhysRevA.52.1875

[17] Sakurai, J.J. (1967) Advanced Quantum Mechanics. Addison-Wesley, Boston.

[18] Jammer, M. (1966) The Conceptual Development of Quantum Mechanics. McGraw-Hill, New York.

[19] Messiah, A. (1961) Quantum Mechanics. John Wiley & Sons, Hoboken.

[20] Grigor'Ev, V.I. (1970-1979) The Great Soviet Encyclopedia. 3rd Edition.

[21] Bender, D., *et al.* (1984) *Physical Review D*, **30**, 515.

[22] Barut, A. and Bracken, J. (1981) *Physical Review D*, **23**, 2454-2463. https://doi.org/10.1103/PhysRevD.23.2454

[23] Hestenes, D. (2008) Reading the Electron Clock.

[24] Rivas, M. (2008) *Journal of Physics A*: *Mathematical and Theoretical*, **41**, Article ID: 304022. https://doi.org/10.1088/1751-8113/41/30/304022

[25] Gouanére, M., *et al.* (2005) *Annales de la Fondation Louis de Broglie*, **30**, 109.

[26] Knuth, K. (2014) *AIP Conference Proceedings*, **1641**, 588. https://doi.org/10.1063/1.4906026

[27] Castelvecchi, D. (2017) *Nature*, **543**, 597-598. https://doi.org/10.1038/543597a

[28] Verlinde, E. (2010) On the Origin of Gravity and the Laws of Newton. https://doi.org/10.1007/JHEP04(2011)029

[29] Silberstein, L. (1907) *Annalen der Physik*, **22**, 579. https://doi.org/10.1002/andp.19073270313

Journal of Modern Physics, 2022, 13, 315-322
https://www.scirp.org/journal/jmp
ISSN Online: 2153-120X
ISSN Print: 2153-1196

Effects of the Nature of Boundaries Conditions and Their Truncation Errors on the Distribution of Minority Carriers in Silicon Solar Cell

Mamadou Bamba Sene[1], Mountaga Boiro[1], Alioune Faye[2], Amadou Diao[1], Cheikh Mbow[2]

[1]Solid State Physics and Materials Sciences Laboratory, Faculty of Sciences and Techniques, University of Cheikh Anta Diop, Dakar, Senegal
[2]Fluid Mechanics and Applied Dynamics System Laboratory, Faculty of Sciences and Techniques, University of Cheikh Anta Diop, Dakar, Senegal
Email: mbsene1@yahoo.fr

How to cite this paper: Sene, M.B., Boiro, M., Faye, A., Diao, A. and Mbow, C. (2022) Effects of the Nature of Boundaries Conditions and Their Truncation Errors on the Distribution of Minority Carriers in Silicon Solar Cell. *Journal of Modern Physics*, **13**, 315-322.
https://doi.org/10.4236/jmp.2022.133022

Received: December 29, 2021
Accepted: March 20, 2022
Published: March 23, 2022

Abstract

In this work, the effects of boundaries conditions and truncation errors in the distribution of minority carriers in the semiconductor are studied. It is a one-dimensional digital study of a polycrystalline silicon solar cell under polychromatic illumination in a dynamic state. Starting from the Boltzmann equation of semiconductors, the author establishes the general equation of particle transport. Assumptions made on the latter allow it to give the equation of distribution of minority carriers in a general way in its case to be studied. This dimensioned distribution equation reveals the parameters of influences on the distribution of carriers. It obtains a partial derivative equation for the carrier distribution function. The boundary conditions are then discretized to order one and then to order two. By considering boundary conditions and the nature of the carriers, the author numerically resolves the discretized general equation by assessing the influence of the nature of the boundary conditions and truncation errors and the influence of the discretization step on the density of the charge carriers by setting certain parameters and varying others. The work ends with a conclusion and logical follow-up to this work.

Keywords

Transport Equation, Load Carrier Densities, Implicit Scheme, Semiconductor, Discretization

1. Introduction

Our daily energy needs have shown that it is impossible to live without energy.

Today, we are constantly witnessing problems linked to insufficient energy production in developed and underdeveloped countries, as well as those linked to the control of the natural energy resources of our universe, linked to many parameters.

These constraints, which can be summed up in its words "socio-economic and ecological constraints", lead to the development of research on renewable energies, which constitute a lasting solution to global energy problems. The latter, in particular photovoltaic energy is a source of hope in the face of the oil crisis, especially for non-oil producing countries. Although global photovoltaic energy production has increased significantly in recent years, its development is still limited by its high cost compared to fossil and nuclear energy.

An accessible way: numerical computation is reserved for mathematicians who are far from the realities of physical phenomena. The physicist must now be able to develop calculation codes to simulate the studied problems. He must have knowledge in numerical analysis in order to rigorously interpret the results of the numerical simulations [1]. It is with this in mind that we have chosen digital analysis as a tool to assess the results of our work. In particular, the effects of the nature of boundary conditions and their truncation errors on the distribution of minority charge carriers in a semiconductor to optimize the yields of photopiles [2]-[7] have been briefly studied.

Thus, to make our contribution in this approach, we propose a modeling of the equation of the distribution of minority carriers in a semiconductor.

2. Mathematical Problem Formulation, Model, Assumptions and Theory

2.1. Mathematical Formulation of the Problem

The modeling of the phenomenon studied consists in taking into account the fundamental principles, such as, for example, the conservation of mass, energy, and in determining the parameters essential to its description both simple and realistic. At each point of the object in question, several physical variables (position, speed, temperature, etc.) describe its state and its evolution and make it possible to fully characterize its movement. These quantities are not independent but are interrelated by equations, which are the mathematical translation of the laws of physics governing the behavior of the object [8] [9].

2.2. Model

A uniformly doped L-length semiconductor was considered. The ionizing radiation is absorbed and generates electron-hole pairs, and $G(x, t)$ is set at the rate of generation of these pairs. The diagram of a particle of the photopile will be shown in **Figure 1**.

2.3. Assumptions

To model carrier transport, we accept that the experiment is carried out in a low

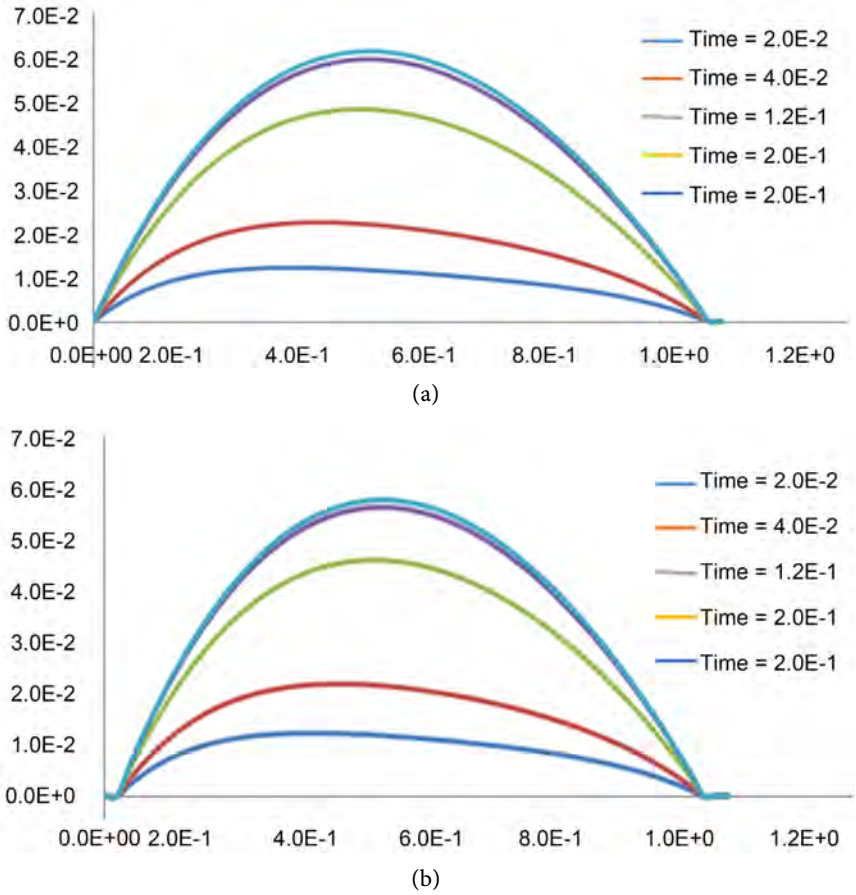

Figure 1. (a) The variation of the number of charge carriers as a function of the discretization step. Change in load carriers according to position x: bil = 0; $a = 1$; $R = 1$; dx = 0.02; (b) The variation of the number of charge carriers as a function of the discretization step. Change in load carriers according to position x: bi0 = 0; $a = 1$; $R = 1$; dx = 0.05.

injection regime in the absence of applied field and assuming that the transport is dominated by diffusion currents. For the resolution we consider the problem to a space dimension.

2.4. Theory

In a type semiconductor, we will high light an electron flow expressed by

$$F = -D\frac{\mathrm{d}\delta}{\mathrm{d}x} \quad [10]\ [11] \tag{1}$$

If we now accept that there is a rate G of generation of electron-hole pairs, a lifetime of which is approximately, that is to say, a recombination rate $[\delta - \delta_0]\ \tau$ or n is the concentration of the instantaneous holes and n_0 is the concentration of the holes which would have at the thermal equilibrium in the absence of any disturbance; therefore the overall balance is obtained in the case of a one-dimensional model [2] [3] [5] [6] [7].

$$\frac{\partial\delta}{\partial t} = D\frac{\partial^2\delta}{\partial x^2} - \frac{\delta - \delta_0}{\tau} + G(x,t) \quad [10]\ [11]\ [12] \tag{2}$$

with:

- δ The density of excess minority charge carriers in the base.
- $G(x, t)$ The rate of generation of charge carriers under illumination.
- D The diffusion coefficient.
- τ The lifetime of excess minority charge carriers.

This equation will be closed by initial conditions and limits that will govern the behavior of the carriers in the semiconductor. In order to generalize our study, we will apply to the geometric limits of our semiconductor conditions to the limits of third type or mixed conditions [8] [9] [10] [11].

The initial conditions:

$$\text{A } t=0 \text{ on a } \quad \delta = \delta_i(x,0) \tag{3}$$

Limit conditions

$$D\left[\frac{\partial\delta(x,t)}{\partial x}\right]_{x=0} = S_f \cdot \delta(0,t) \tag{4}$$

$$D\left[\frac{\partial\delta(x,t)}{\partial x}\right]_{x=L} = -S_b \cdot \delta(L,t) \quad [12] [13] [14] \tag{5}$$

- S_f The recombination speed at the junction of the excess minority charge carriers of the front-side illuminated photopile.
- S_b The recombination speed of excess minority charge carriers at the rear face when the front face is illuminated.
- L is the length of the photocell.

3. Results and Discussions

In this section, we will present the results of the numerical simulations and discuss the influence of the nature of the boundary conditions and their discretization errors on the behavior of the charge carriers.

The results discussed here are relative

3.1. Sensitivity of Results with Respect to Discretization Steps

To choose the "optimum", we tested the sensitivity of the results with respect to the calculation steps. The analysis of the curves of **Figure 1** shows that the results obtained for spacing steps of 0.05 and 0.02 are substantially the same. Therefore, it is useless to work with space pitches greater than 0.02 because we will have a greater volume of calculations and a longer execution time and finally have the same results as those of **Figure 1(b)**.

3.2. Overall Analysis of the Behavior of the Charge Carriers

Figure 2 and **Figure 3** show that the steady state begins to be reached when the adimensional time is greater than or equal to 0.2. When Dirichlet conditions are imposed on the limits of our semiconductor, the increase in the power of the incident radiation simply results in an increase in the maximum of the load carriers but the curves remain the same as we can see on the curves of **Figure 3**. On

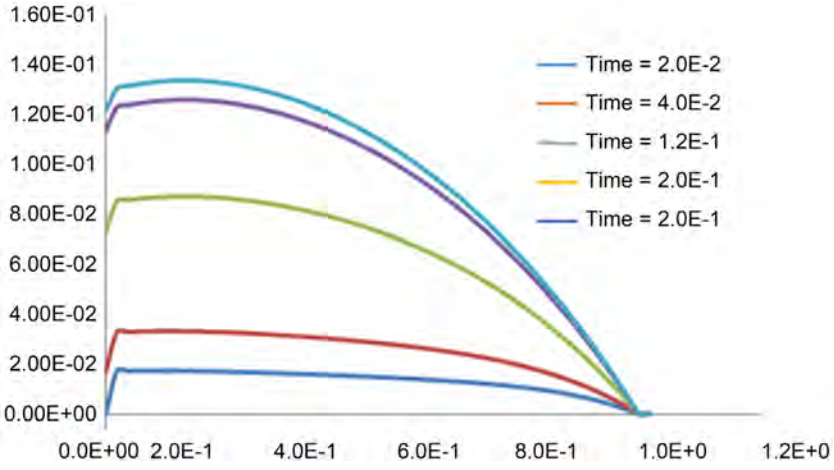

(a)

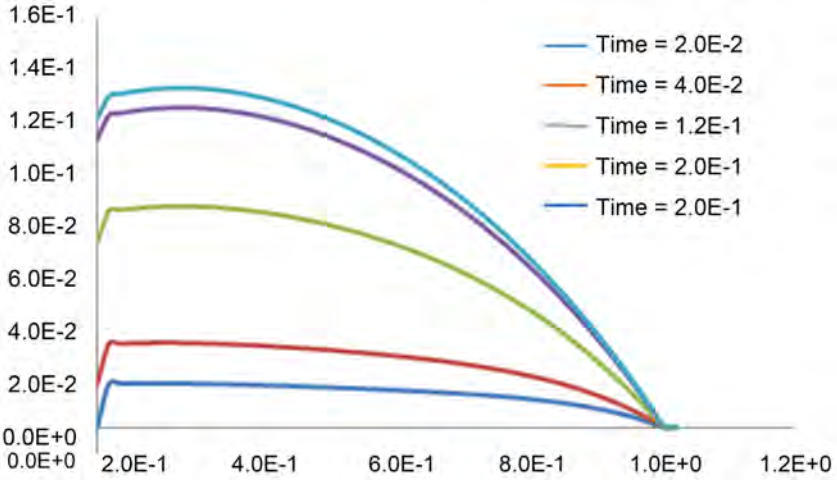

(b)

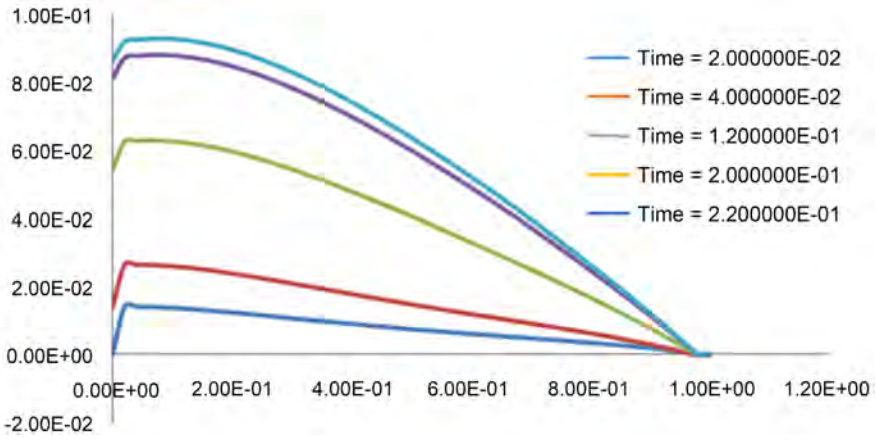

(c)

Figure 2. (a) The change in the number of charge carriers as a function of the absorption coefficient α. Change in load carriers according to position x: bi0 = 2; $\alpha = 0.1$; $R = 1$; dx = 0.1; (b) The change in the number of charge carriers as a function of the absorption coefficient α. Change in load carriers according to position x: bi0 = 2; $\alpha = 1$; $R = 1$; dx = 0.1; (c) The change in the number of charge carriers as a function of the absorption coefficient α. Change in load carriers according to position x: bi0 = 2; $\alpha = 2$; $R = 1$; dx = 0.1.

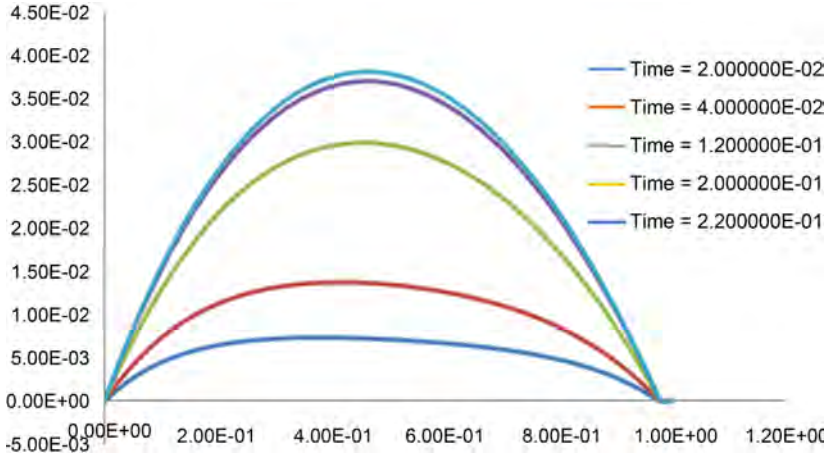

(a)

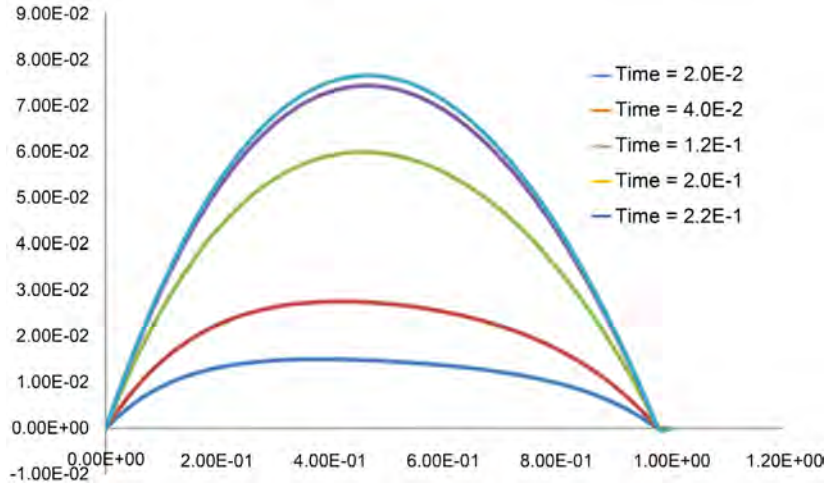

(b)

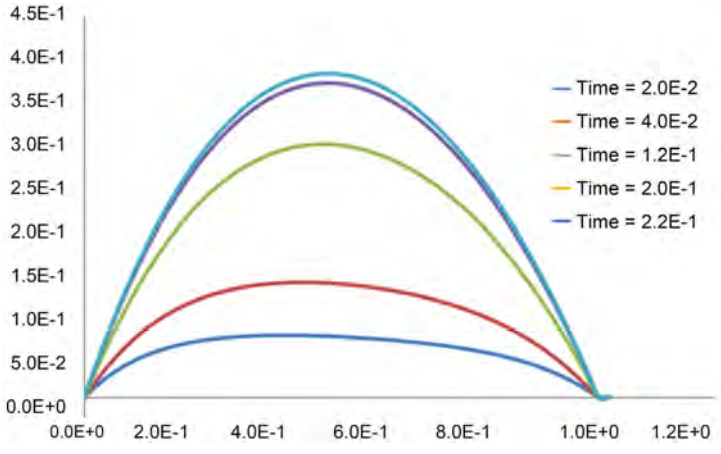

(c)

Figure 3. (a) The variation in the number of load carriers as a function of the incident Power *R*. Change in load carriers according to position x: bi0 = 2; $\alpha = 0.1$; $R = 0.5$; dx = 0.1; (b) The variation in the number of load carriers as a function of the incident Power *R*. Change in load carriers according to position x: bi0 = 2; $\alpha = 0.1$; $R = 1$; d$x = 0.1$; (c) The variation in the number of load carriers as a function of the incident Power *R*. Change in load carriers according to position x: bi0 = 2; $\alpha = 0.1$; $R = 0.5$; d$x = 5$.

the other hand, an increase in the absorption coefficient of the material causes a reduction in the values of the maximum carriers as shown by the curves of Figure 2.

Thereafter, the following results will relate to a space step of 0.02, that is to say of 1/50.

- dx the discretization step;
- α the absorption coefficient;
- R the incident power.

4. Conclusions

This work is a modeling study of the effects of the natures of boundary conditions and their truncation errors on the distribution of minority carriers in a semiconductor.

A mathematical study of the load carrier distribution equation and boundary conditions was used to model the distribution of minority carriers in a semiconductor. This model is based on Thomas' method and the scheme used is the implicit scheme. However, we studied the influence on load carrier distribution, discretization of boundary conditions, and semiconductor characteristics.

It should be noted that the method used is rapid and allowed us to appreciate the influence of the discretization of boundary conditions and the nature of boundary conditions. In this work, we have punctuated the influence or not on the number of diffused carriers of the characteristics of the material. Here, a simple case was considered; there are parameters that are not considered. Thus, it is conceivable to make a complete study of the photopile while taking into account the real values of its characteristics, taking into account the speeds of recombination, currents, etc.

Conflicts of Interest

The authors declare no conflicts of interest regarding the publication of this paper.

References

[1] Mbow, B., *et al.* (1994) *Physica Status Solidi* (*a*), **141**, 511-525. https://doi.org/10.1002/pssa.2211410231

[2] Sze, S.M. and Kwok, K.N. (2006) *Physics of Semiconductor Devices*, **10**, 5-75.

[3] Grove, A.S. (1967) Intel Corporation, Mountain View Physics and Technology of Semiconductor Devices. 366 p.

[4] Poupaud, F., Rascle, M. and Vila, J.P. (1995) *Journal of Differential Equations*, **123**, 93-121.

[5] Peaceman, D.W. and Rachfort, H.H. (1955) *Journal of the Society for Industrial and Applied Mathematics*, **3**, 28-41.

[6] Nogotov, E.F. (1978) Applications of Numerical Heat Transfer. Mc Graw Hill Book Company, New York.

[7] Press, W.H., Teukolsky, S.A., Vetterling, W.T. and Flannery, B.P. (1992) Recettes

numériques en Fortran. 2e Édition, Chapitre 16, Cambridge University Press, Cambridge.

[8] Luz, T.D., Battisti, F.G. and da Silva, A.K. (2022) *International Journal of Computation and Methodology*, **81**, 3-6.

[9] El Ghitani, H. and Martinizzi, S. (1989) *Journal of Applied Physics*, **66**, 1723-1726. https://doi.org/10.1063/1.344393

[10] Sène, M.B., Diao, A., Faye, A. and Mbow, C. (2021) *American Journal of Modern Physics*, **10**, 55-59. https://doi.org/10.11648/j.ajmp.20211003.13

[11] Zoungrana, M., Zerbo, I., Barro, F.I., Sam, R., Touré, F., Samb, M.L. and Zougmoré, F. (2011) *Renewable Energy Review*, **14**, 649-664.

[12] Zerbo, I., Zoungrama, M., Seré, A.D., Ouedraogo, F., Sam, R., Zouma, B. and Zougmoré, F. (2011) *Renewable Energy Review*, **14**, 517-532.

[13] Mbodji, S., Zoungrana, M., Biram, I.Z. and Sissoko, G. (2015) *World Journal of Condensed Matter Physics*, **5**, 284-293. https://doi.org/10.4236/wjcmp.2015.54029

[14] Thiam, N., Diao, A., Wade, M., Ndiaye, M., Zerbo, I., Sarr, M., Maîga, A.S. and Sissoko, G. (2013) *Research Journal of Applied Sciences, Engineering and Technology*, **5**, 134-141. https://doi.org/10.19026/rjaset.5.5137

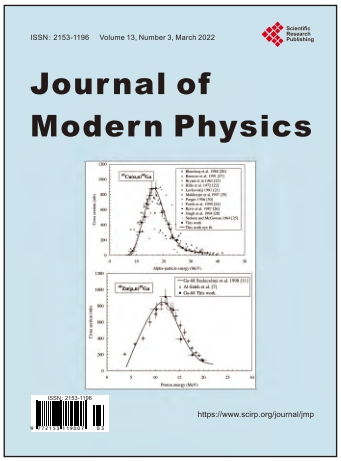

Call for Papers

Journal of Modern Physics

ISSN: 2153-1196 (Print) ISSN: 2153-120X (Online)
https://www.scirp.org/journal/jmp

Journal of Modern Physics **(JMP)** is an international journal dedicated to the latest advancement of modern physics. The goal of this journal is to provide a platform for scientists and academicians all over the world to promote, share, and discuss various new issues and developments in different areas of modern physics.

Editor-in-Chief

Prof. Yang-Hui He City University, UK

Subject Coverage

Journal of Modern Physics publishes original papers including but not limited to the following fields:

Biophysics and Medical Physics
Complex Systems Physics
Computational Physics
Condensed Matter Physics
Cosmology and Early Universe
Earth and Planetary Sciences
General Relativity
High Energy Astrophysics
High Energy/Accelerator Physics
Instrumentation and Measurement
Interdisciplinary Physics
Materials Sciences and Technology
Mathematical Physics
Mechanical Response of Solids and Structures
New Materials: Micro and Nano-Mechanics and Homogeneization
Non-Equilibrium Thermodynamics and Statistical Mechanics
Nuclear Science and Engineering
Optics
Physics of Nanostructures
Plasma Physics
Quantum Mechanical Developments
Quantum Theory
Relativistic Astrophysics
String Theory
Superconducting Physics
Theoretical High Energy Physics
Thermology

We are also interested in: 1) Short Reports—2-5 page papers where an author can either present an idea with theoretical background but has not yet completed the research needed for a complete paper or preliminary data; 2) Book Reviews—Comments and critiques.

Notes for Intending Authors

Submitted papers should not have been previously published nor be currently under consideration for publication elsewhere. Paper submission will be handled electronically through the website. All papers are refereed through a peer review process. For more details about the submissions, please access the website.

Website and E-Mail

https://www.scirp.org/journal/jmp **E-mail: jmp@scirp.org**

What is SCIRP?

Scientific Research Publishing (SCIRP) is one of the largest Open Access journal publishers. It is currently publishing more than 200 open access, online, peer-reviewed journals covering a wide range of academic disciplines. SCIRP serves the worldwide academic communities and contributes to the progress and application of science with its publication.

What is Open Access?

All original research papers published by SCIRP are made freely and permanently accessible online immediately upon publication. To be able to provide open access journals, SCIRP defrays operation costs from authors and subscription charges only for its printed version. Open access publishing allows an immediate, worldwide, barrier-free, open access to the full text of research papers, which is in the best interests of the scientific community.

- High visibility for maximum global exposure with open access publishing model
- Rigorous peer review of research papers
- Prompt faster publication with less cost
- Guaranteed targeted, multidisciplinary audience

Scientific Research Publishing

Website: https://www.scirp.org

Subscription: sub@scirp.org

Advertisement: service@scirp.org